UNIVERSITY OF OKLAHOMA

GRADUATE COLLEGE

# INDIUM ARSENIDE/GALLIUM ARSENIDE ANTIMONIDE QUANTUM DOTS AND THEIR APPLICATIONS IN INTERMEDIATE BAND SOLAR CELLS

A THESIS

SUBMITTED TO THE GRADUATE FACULTY

in partial fulfillment of the requirements for the

Degree of

MASTER OF SCIENCE

By

ANTHONY JAMES MELECO
Norman, Oklahoma
2016

Downloaded from SHAREOK. Persistent Handle URL: https://hdl.handle.net/11244/42984

INDIUM ARSENIDE/GALLIUM ARSENIDE ANTIMONIDE QUANTUM DOTS AND THEIR APPLICATIONS IN INTERMEDIATE BAND SOLAR CELLS

A THESIS APPROVED FOR THE
DEPARTMENT OF ENGINEERING PHYSICS

BY

_____
Dr. Ian R. Sellers, Chair

_____
Dr. Patrick J. McCann

_____
Dr. Lloyd A. Bumm

© Copyright by ANTHONY JAMES MELECO 2016
All Rights Reserved.

## Acknowledgments

I would like to first begin by thanking Dr. Ian Sellers for both his knowledge and patience. There have been too many times where I did not stay on task and finish things in a timely manner and he always encouraged me to get back on track. It is because of him that this thesis and project has been completed within a reasonable time frame. I do not think I could have picked a better adviser and I am grateful to have gotten a chance to work with him and know him. I will miss his humor and British accent in my future endeavors.

I would like to thank Dr. Vincent Whiteside for his many, many answers to my questions and help over the years. He is maybe the most patient person I have ever met and it has truly been an honor to get to know him. I will miss our random conversations in his office.

I would also like to thank Dr. Bumm and Dr. McCann for serving as my committee members and taking time out of their life to read this thesis and for giving me additional time to finish editing.

Thanks to Dr. Mukul Debnath of Dr. Santos' group for growing the samples.

Thanks to my collaborators on this project at Amethyst Research Inc. and University College of London and thanks to OCAST for initial funding of this project.

Next, I would like to thank my parents for always being there for me, listening to me vent, encouraging me and never letting me give up on anything I do.

Lastly, thanks to all the friends I've made over the years for making this experience an incredible 8 years of undergraduate and masters studies. I could not have made it through without you guys!

# Table of Contents

Acknowledgments ..... iv

List of Figures ..... vii

Abstract ..... ix

Chapter 1: Introduction ..... 1

1.1 Today's Energy Landscape ..... 1

1.2 The History of Solar Cell Research ..... 4

1.3 The Three Generations of Solar Cell Research ..... 4

Chapter 2: Solar Cell Operation and Efficiency ..... 8

2.1 Solar Cell Operation and Junctions ..... 8

2.2 The Efficiency Limit of Solar Cells ..... 13

2.3 Methods to Exceed the Shockley-Queisser Limit ..... 19

Chapter 3: Intermediate Band Solar Cells ..... 21

3.1 Concept ..... 21

3.2 Creating an Intermediate Band ..... 21

Chapter 4: Investigation into Four InAs/GaAsSb Devices ..... 25

4.1 Characterization of Solar Cells ..... 25

Photoluminescence Spectroscopy ..... 25

External Quantum Efficiency ..... 26

Current-Voltage Analysis ..... 27

4.2 Experimental Design and Setup ..... 30

Sample Growth ..... 30

Sample Preparation ..... 32

IV Measurement Experimental Setup ..... 33
EQE Measurement Experimental Setup ..... 35
PL Measurement Experimental Setup ..... 37
4.3 Experimental Results and Discussion ..... 39
Low-temperature Photoluminescence ..... 39
Low-temperature External Quantum Efficiency ..... 44
Temperature Dependent External Quantum Efficiency ..... 47
Temperature Dependent Photoluminescence ..... 49
Current Density-Voltage Analysis ..... 52
Open-circuit Voltage Analysis ..... 55
Short-circuit current Analysis ..... 56
Temperature dependent dark current-voltage Analysis ..... 56
Chapter 5: Conclusion ..... 62
References ..... 63

# List of Figures

Figure 1. World Energy Supply ..... 1

Figure 2. Average Cost of Utility-Scale PV Systems in the United States ..... 2

Figure 3. Current LCOE of Technologies in the United States ..... 3

Figure 4. PV Production by Technology per Year ..... 5

Figure 5. Thin-Film Market Share by Year ..... 6

Figure 6. Efficiency and Cost Projections for the Three Generations of Solar ..... 7

Figure 7. p-n Junction ..... 10

Figure 8. p-i-n junction ..... 11

Figure 9. Type-I and Type-II Band Alignment ..... 12

Figure 10. Optical Depth of the Atmosphere ..... 14

Figure 11. Solar Spectrum ..... 15

Figure 12. Shockley Queisser limit and Semi-Empirical Limit ..... 16

Figure 13. Intrinsic Losses in a Solar Cell as a Function of Band Gap ..... 17

Figure 14. Loss Processes in a Standard Solar Cell ..... 18

Figure 15. Intermediate Band Solar Cell Band Diagram ..... 22

Figure 16. Equivalent Circuit of Model ..... 29

Figure 17. Device Structure for a Sample Containing One Layer of QDs ..... 31

Figure 18. Two of the Solar Cell Samples ..... 32

Figure 19. Linkam Micro Cryostat ..... 33

Figure 20. IV Experimental Setup ..... 34

Figure 21. EQE Experimental Setup ..... 36

Figure 22. Continuous EQE Meter ..... 37

Figure 23. PL Experimental Setup ..... 38
Figure 24. 4.2 K Norm. PL with Logged Inset ..... 40
Figure 25. 4.2 K Logged Power Dependence ..... 42
Figure 26. PD Peak Energy vs Power$^{1/3}$ ..... 43
Figure 27. Band Alignment of QD Samples ..... 44
Figure 28. EQE 77 K ..... 45
Figure 29. Logged TD EQE ..... 48
Figure 30. Logged TD PL ..... 49
Figure 31. Peak Data for Layered Samples ..... 51
Figure 32. 77 K J-V ..... 52
Figure 33. 300 K J-V ..... 53
Figure 34. Temperature Dependent $V_{oc}$ ..... 54
Figure 35. Temperature Dependent $J_{sc}$ ..... 55
Figure 36. Temperature Dependent Jdark-V Measurements ..... 57
Figure 37. Example of Fits in Control ..... 58
Figure 38. Dark Saturation Current Coefficients ..... 59
Figure 39. Barrier Extraction of Dark Currents ..... 60

# Abstract

This thesis briefly presents the current energy production landscape and where photovoltaics stand relative to other technologies. The history of the field is introduced as well as current research - most notably third generation solar cell technologies and their potential to lead to higher efficiencies and lower cost compared to today's dominant crystalline silicon technologies. Quantum dot intermediate band solar cells (QD IBSCs), in particular, are examined as well as experimental results of four InAs/$GaAs_{.86}Sb_{.14}$ QD IBSCs. InAs QDs have potential, but due to material quality of the main material system, show no evidence of an isolated intermediate band and quantum confinement, a necessary component of a workable IBSC.

# Chapter 1: Introduction

## 1.1 Today's Energy Landscape

As the world population continues to increase, world energy demands have been rising globally to match it. These demands have been met mostly by the non-renewable sources such as oil, coal and natural gas. In 2013, those sources contributed to 81.4% of the world's energy production [1].

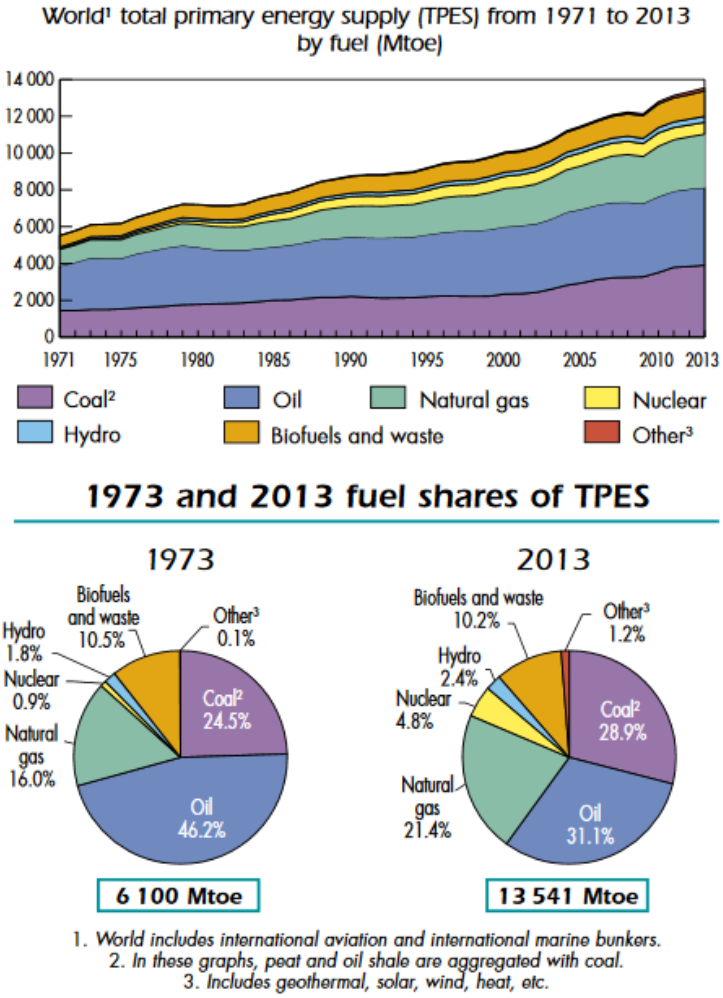
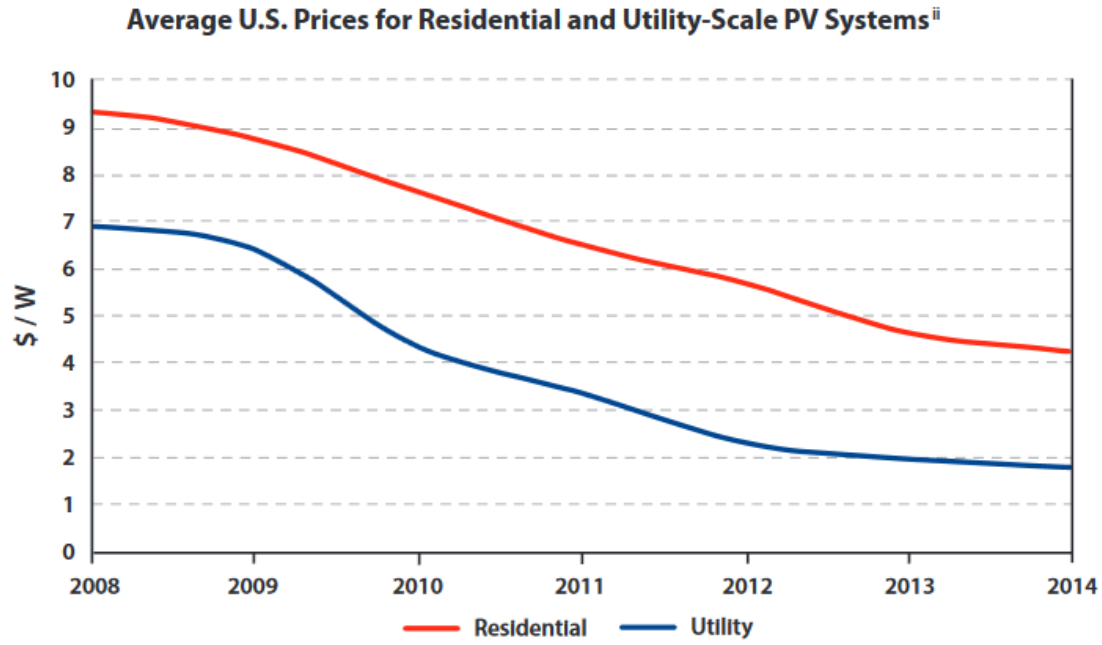



**Figure 1. World Energy Supply**
Top figure: Energy source by year in units of MToe, mega tonne of oil equivalent, (1 GWh = 0.000086 Mtoe). Bottom figure: Percentages of energy sources of TPES (total primary energy supply)
*2015 Key World Energy Statistics, 1st ed. Paris: IEA Publishing, 2015, p. 6.*




[ii] MIT analysis based on data Solar Industry Association of America; NREL; Barbose, Weaver, and Darghouth; NREL; and Feldman, Margolis, and Boff.

**Figure 2. Average Cost of Utility-Scale PV Systems in the United States**
Residential (red) and utility-scale pv systems (blue) cost in units of dollar/watt from 2008-2014
*The Future of Solar Energy: An Interdisciplinary MIT Study, 1st ed. Massachusetts Institute of Technology, 2015, p. xiii-xviii, 80.*

However, the use of non-renewable energies, specifically fossil fuels, along with the processes used to extract them have had strong negative effects on the environments that house them [2][3]. Additionally, mounting evidence supports the idea that usage of these energies has an effect on the entire world in the form of global warming or climate change [4].

Several ideas have been proposed to prevent further environmental damage. Chief among these ideas is the usage of a different energy source that does not have a negative impact on the environment [5]. Solar energy has long been a candidate for a renewable energy source because of the large amount of energy that is incident on Earth on any given day [6] [7]. However, in locations such as the United States [7] solar energy as a technology has not made sense commercially due to cost until recently, with

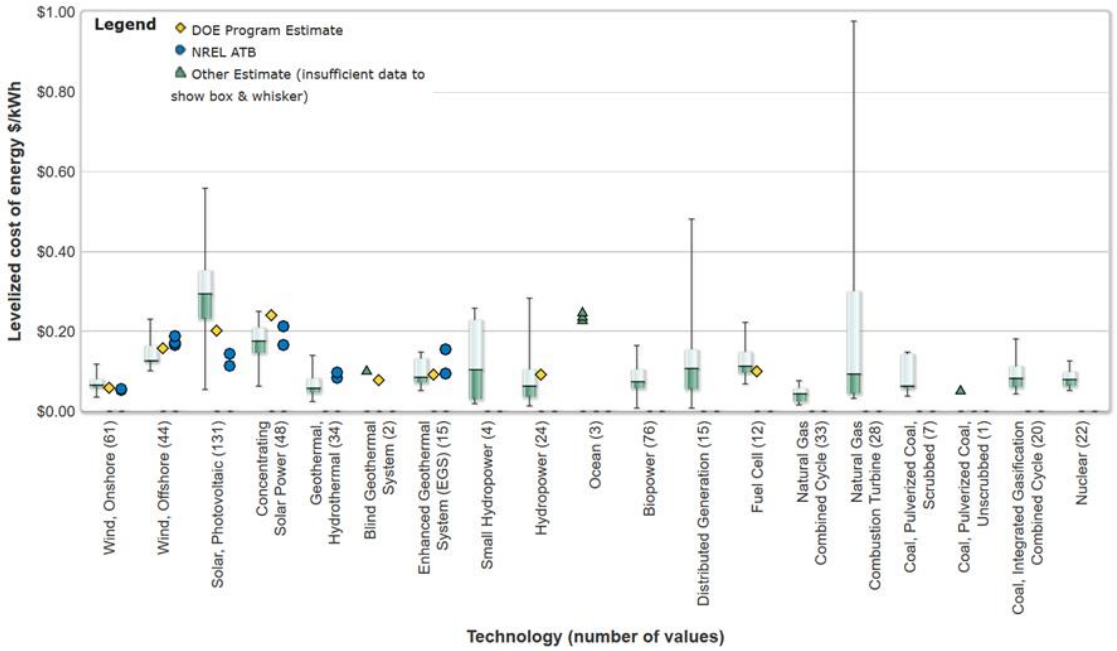



**Figure 3. Current LCOE of Technologies in the United States**
Different levelized cost of energy (LCOE) are presented here for various technologies in units of dollar/kilowatt*hour. Solar energy and concentrated solar energy are listed third and fourth respectively. Range of cost is noted by box and whiskers. Other estimates are noted by symbols in the legend.
*"NREL: Energy Analysis - Levelized Cost of Energy Calculator", Nrel.gov, 2016. [Online]. Available: http://www.nrel.gov/analysis/tech_lcoe.html. [Accessed: 13- May- 2016].*

costs getting closer to competitive pricing in the United States; this is shown in Figure 2: describing average cost of utility scale PV systems in the US [8] and Figure 3: showing solar energy when compared with other energy technologies [9]. These trends, thought to continue with the introduction of newer technologies, are currently contributed to falling module prices, as well as, falling prices of the current predominant technology: wafer-based crystalline silicon. In other parts of the world, solar cells have already achieved grid parity with other energy sources; but, further research on newer technologies, as well as, government subsidies will be needed if solar is ever to become the world leader as an energy source [8].

## 1.2 The History of Solar Cell Research

Research on solar cells as they are known today did not start until recently in human history but, the idea behind them – conversion of energy – has been around since antiquity. Thousands of years ago people realized that sunlight and heat were related and were able to build the first focusing lenses to create fire. That relation built on itself with several useful inventions since then that trapped sunlight in unique ways; enabling the materials that trapped it to absorb more sunlight and direct it so that it could be used to heat homes or cook food. It was not until 1839 when Edmond Becquerel realized that sunlight could be converted to something other than heat: electricity, with the creation of what came to be known as the photovoltaic effect [10] [11]. This effect, the generation of a potential from light, was then discovered and used in selenium cells in the late 1800's [10].

In the next 100 years: the photoelectric effect was discovered by Heinrich Hertz and later explained using quantum mechanics by Albert Einstein; the first semiconductor junction solar cell (copper/copper oxide) was created; other materials were investigated as producing the photovoltaic effect; then, in 1954 Bell Labs invented the first practical silicon cell with 6% efficiency [10][11]. While these cells were inefficient and expensive, roughly 200 dollars per watt, the promise of power generation, as well as, the potential for applications not yet seen by conventional energy generation drove future research [11].

## 1.3 The Three Generations of Solar Cell Research

Bell Labs' invention of a practical silicon solar cell started what is known as the first generation of solar cell research. This generation is composed of mostly bulk

crystalline silicon and the refining processes that ultimately determine the quality or purity of the silicon. It focuses on single p-n junction research and the dopants to create them. Crystalline silicon research itself is split into multicrystalline silicon and monocrystalline silicon. Mono-Si is the purer of the technologies and has higher efficiencies (up to 25.6% today) than other forms of silicon but is also more expensive. Multi-Si, named so because it is not composed of a single crystalline structure, is cheaper, easier to produce and has lower efficiencies (20.4%). Production in 2014 favored Multi-Si (Figure 4 [12]) because of its cost per watt ratio due to its abundance and maturity as a technology [12].

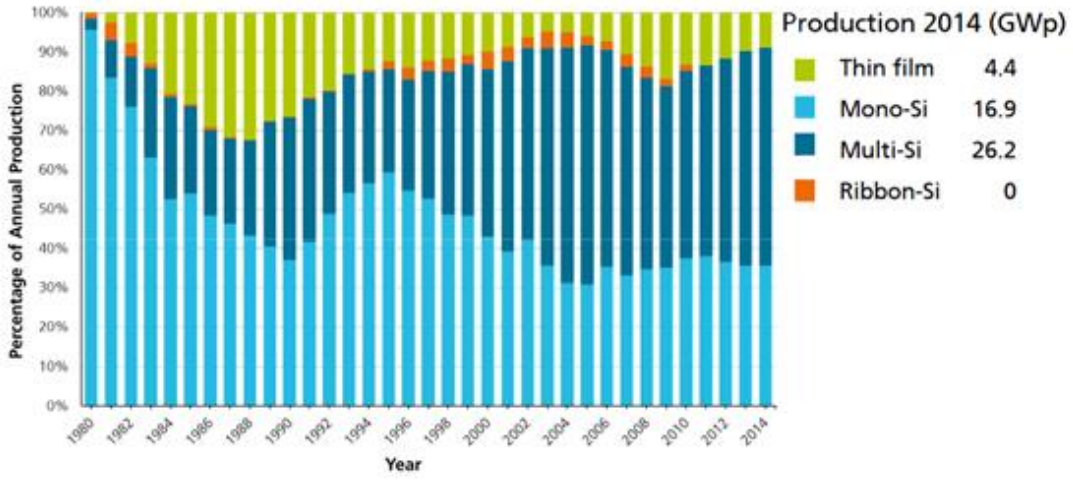



**Figure 4. PV Production by Technology per Year**
Composition of main technologies that comprise PV production by year from 1980 to 2014. Also listed is the GWp, peak energy produced (gigawatts) of the technologies worldwide.
*PHOTOVOLTAICS REPORT, 1st ed. Frieburg: Fraunhofer Institute for Solar Energy Systems, ISE, 2016, pp. 19-20.*

In the late 1970s and early 1980s, the first thin film solar cells were developed [10]. These thin film solar cells consist of the second generation of solar cells and they are comprised of several different types of solar cells such as: cadmium telluride, copper indium gallium diselenide (CIGS), and amorphous thin-film silicon. This

technology was developed because traditional, first generation silicon cells were thick (200 micrometers) relative to these technologies. Using less material meant that these cells were less costly per watt, despite being less efficient [12].

Today, use of these technologies are limited due to toxicity and rarity of the materials affecting public opinion, as well as, the price of crystalline silicon continuing to fall. Additionally, some companies producing thin film cells have shut down research or gone bankrupt [13]. Despite this, thin film technologies like CdTe are still considered a large business within the solar industry; the thin film industry (Figure 5 [12]) and companies like First Solar still champion the technology [14].

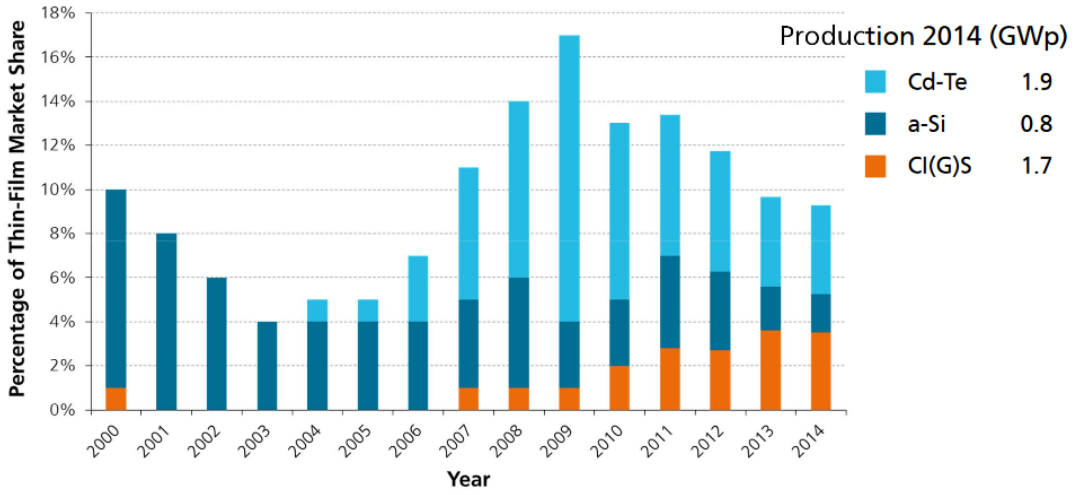



**Figure 5. Thin-Film Market Share by Year**
The thin-film market from figure 4 is broken down into its components for the years 2008-2014. Their total capacity worldwide is also listed in GWp.
*PHOTOVOLTAICS REPORT, 1st ed. Frieburg: Fraunhofer Institute for Solar Energy Systems, ISE, 2016, pp. 19-20.*

Today's most fundamental research lies in third generation solar cells [15]. These solar cells consist of any technology that is theoretically able to achieve high efficiencies for less cost than other technologies, perhaps even above a theoretically calculated limit known as the Shockley-Queisser limit [15] [16], possibly utilizing thin-

film deposition methods of the second generation. Figure 6 summarizes all these technologies in terms of efficiencies vs. cost projections [17].

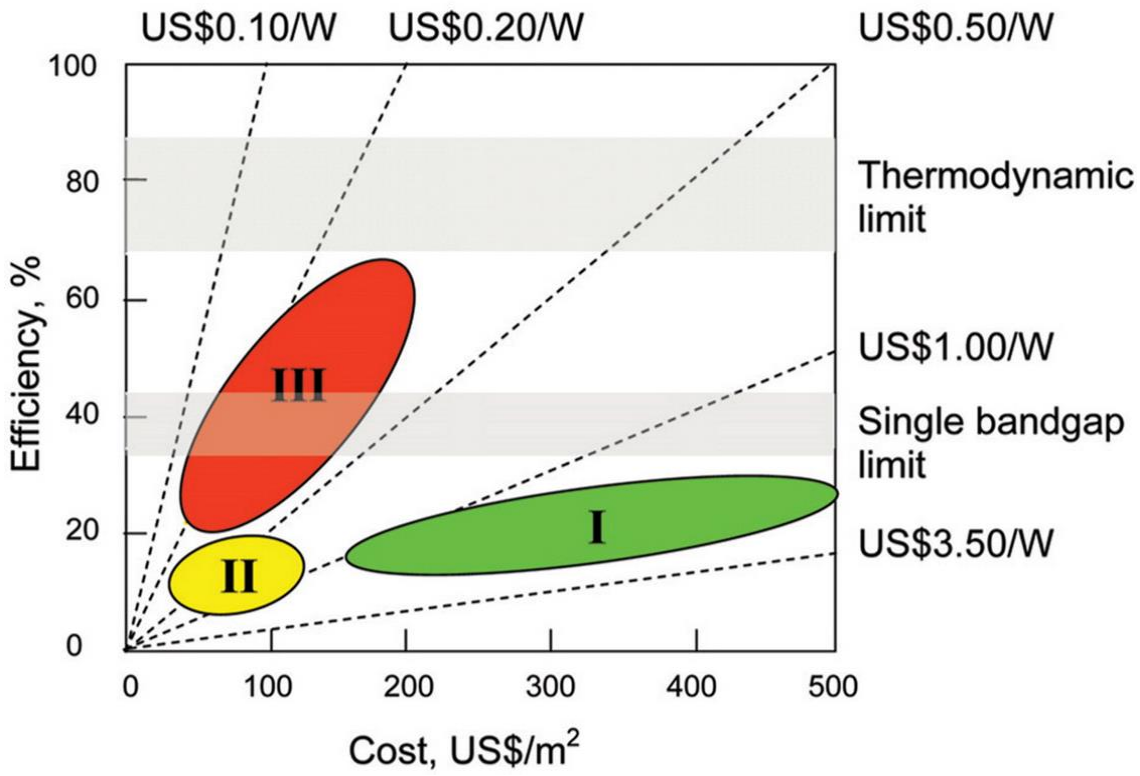



**Figure 6. Efficiency and Cost Projections for the Three Generations of Solar**
Range of efficiency per cost of the three generations of solar cell research are presented in green (gen I), yellow (gen II) and red (gen III). For comparison, the single band gap and thermodynamic limit are listed. The dotted lines serve as a guide for where different costs/Watt lay relative to these technologies.
*G. Conibeer, "Third-generation photovoltaics", Materials Today, vol. 10, no. 11, pp. 42-50, 2007.*

# Chapter 2: Solar Cell Operation and Efficiency

## 2.1 Solar Cell Operation and Junctions

All solar cells work through their ability to absorb photons of different energies due to the photovoltaic effect, as well as, the extraction of carriers excited from that absorption; a carrier is either an electron or a hole, the hole being the collective response due to the absence of an electron. The device, if connected to a load, then produces a current with the extracted carriers generating power and then can be reused once they cycle back into the system [11].

To accomplish this, many factors should be considered starting with the materials involved. Many different material systems can create a solar cell with the most common being systems derived from semiconductor elements. Semiconductors are used because they possess many interesting properties that conductors or insulators do not have, such as variable resistance, which is a function of the separation of "bands" in the material, known as a band gap. These bands, formed from the overlap of the atomic orbitals of the elements in the material, dictate where states of an electron can exist and so determine the overall voltage of the device, as well as, the effectiveness of the solar cell. The band theory of solids, as it has come to be known, is used to determine many different properties, such as absorption, of not only solar cells, but most solid state devices like the transistor and thus has been instrumental in the understanding of these devices [11].

There are two bands out of an infinite number in a solid worth noting that influence the resistance of the material: the valence (VB) and conduction band (CB). These are the two bands that influence conductivity due to their proximity to each other.

A larger band gap may result in an insulator, while a band gap of zero results in a conductor. The VB is generally filled with more electrons than the CB, though this can vary with temperature. At absolute zero, when the electrons occupy the lowest available states, the energy up to which states are filled is known as the Fermi energy. At higher temperatures, the electrons can fill higher energy states. The Fermi level, named after Enrico Fermi, is the average probability of state being occupied by an electron at a given temperature [11].

One can shift the Fermi level through the use of impurities. Intentionally adding impurities is known as doping and there are two ways one can dope a material. P-type doping involves the use of elements with less electron density than the main material system. N-type doping adds electron density to the material. As stated before - doping influences the Fermi level - when differing Fermi levels are put together in a material an imbalance known as a p-n junction [11] is created. Figure 7 part (a) visualizes the fixed ions created when materials with different dopants are brought together. Part (b) shows the important electron energy levels (in equilibrium) as a function of their spatial location at the junction. This is otherwise known as a band diagram and is helpful in the understanding of different junctions.

The p-n junction is essential to the operation of a solar cell, as well as, most solid state devices. The interface formed from the boundary of differently doped materials assists in carrier extraction by means of the E-field present across the interface region. This region, known as: the space charge region varies by doping concentration, develops due to diffusion. Carriers that diffuse from an n-doped part of the cell to the p-

doped part of the cell leave behind the opposite charge, which becomes the fixed ions previously mentioned.

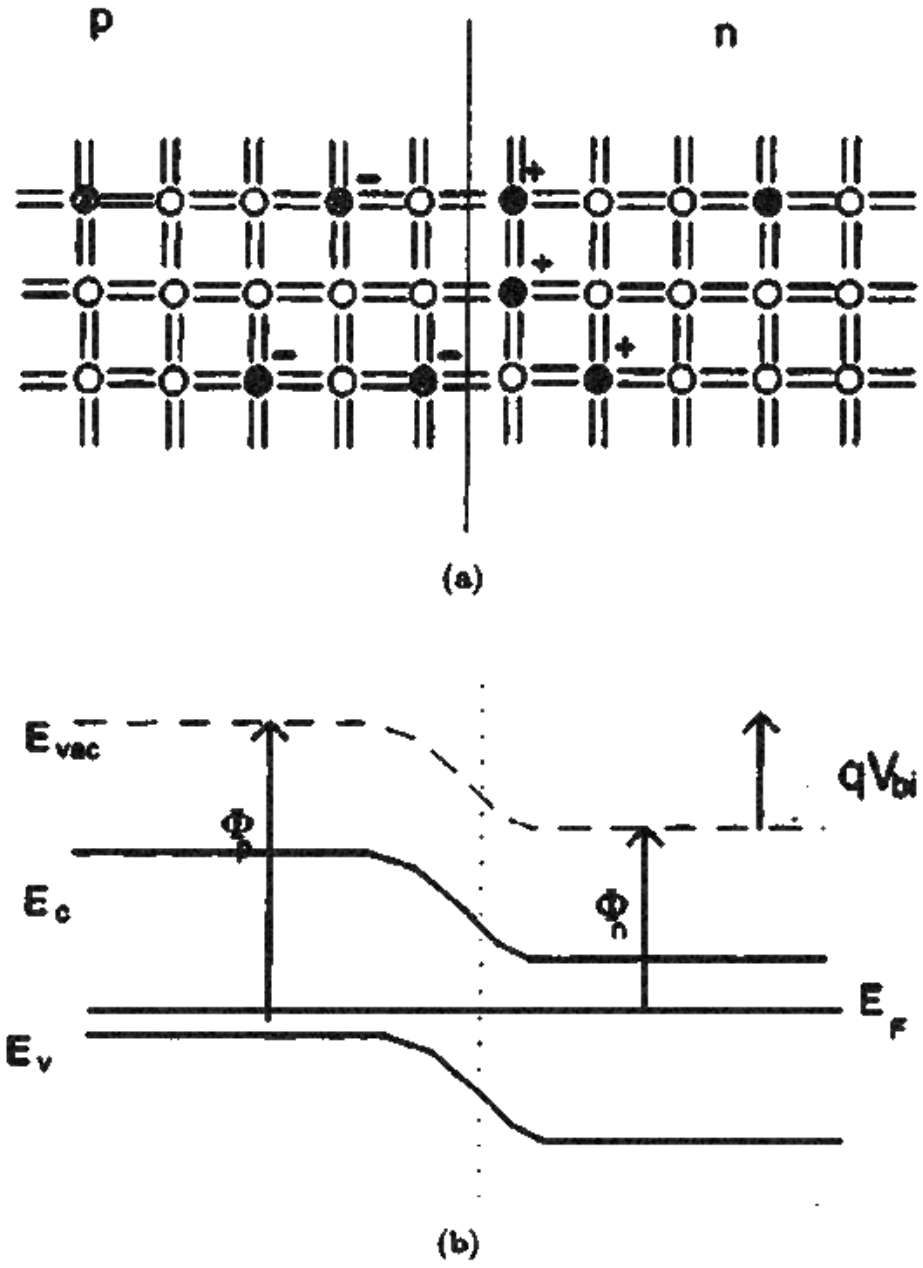



**Figure 7. p-n Junction**
Part (a): Fixed ions near junction. Part (b): Band diagram (plotted as Energy vs spatial location) near a p-n junction. $\Phi_p$ and $\Phi_n$ represent the work functions of the p and n regions respectively. $V_{bi}$ is the built in voltage while *q* is the charge of an electron. The energy levels are conduction, valence, Fermi and evac, the energy where carriers are free from any forces in the solid
*J. Nelson, The physics of solar cells. London: Imperial College Press, 2003.*

Eventually, this diffusion stops completely due to the build-up of that opposite fixed charge. Decreasing this E-field with an applied bias results in diffusion once again; it is considered majority carrier diffusion since it is the majority carriers, i.e., the most abundant carriers that determine the current flow. A solar cell under these conditions operates as a diode. Under illumination, however, light generation of carriers causes the device to produce current through minority carriers. If the device is connected to a load, the carriers can flow through the device producing useful electrical work [11].

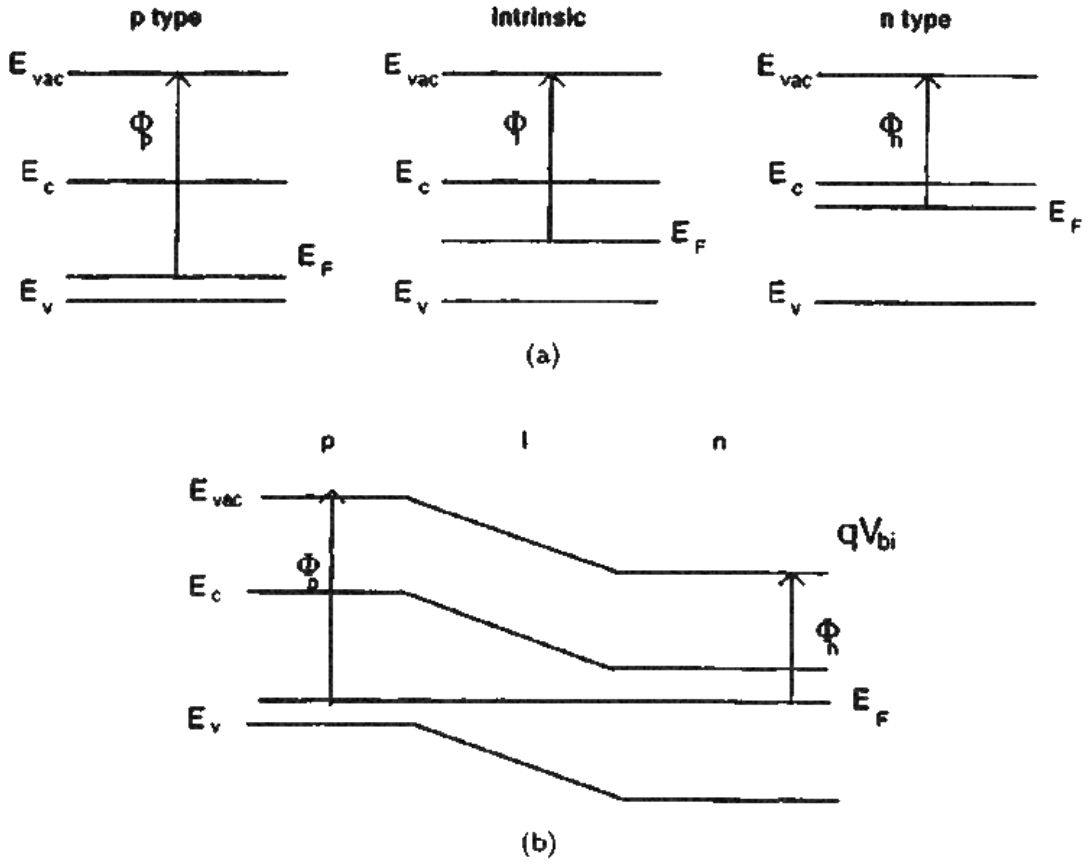



**Figure 8. p-i-n junction**
Part (a): p, i, n bands in isolation. Part (b): Band diagram of the p-i-n junction
*J. Nelson, The physics of solar cells. London: Imperial College Press, 2003.*

The p-n junction is the simplest type of junction. Another of interest is a p-i-n structure which adds an intrinsic region with no doping in between the p and n doped regions. One advantage noted for this structure is that it extends the thickness of the device to further increase photon absorption in systems where carrier lifetimes are shorter [11]. The junction's band profile and its components are shown in Figure 8 on the previous page.

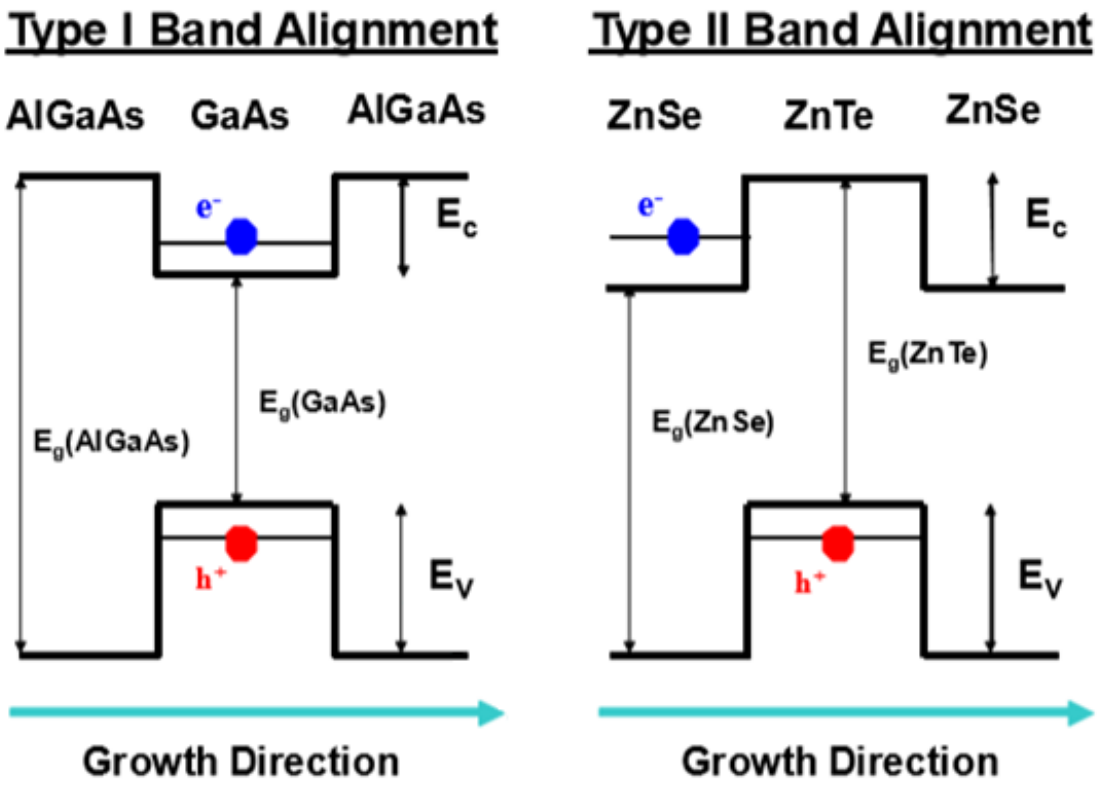



**Figure 9. Type-I and Type-II Band Alignment**
The left structure forms a type-I band alignment through the use of the narrow band gap GaAs being sandwiched between the wider band gap AlGaAs. This forms a quantum well for both the electron and hole. The confinement is represented a horizontal line. In the right structure, an example of type-II is given through the use of a ZnTe QD confining the hole to one side of the junction. On the other side of the junction is the electron that is bound to the hole through coulombic attraction
*V. Whiteside, The optical Aharonov-Bohm effect and magneto-optical properties of type-II quantum dots. 2011.*

The previous two junctions discussed (and examples used) are known as homo-junctions since the material involved on each side of the junction is the same material.

Additionally, hetero-junctions exist when dissimilar materials come in contact with each other. Just how the different materials affect the energy bands determines the type of hetero-junction that forms. The two main categories are type-I and type-II. In type-I, a narrow band gap material is sandwiched between a wider band gap material creating one side of the heterojunction that is a lower energy for both the electrons and holes. This can create confinement hindering transport, while radiative recombination is larger. In type-II band alignment, lower energy for the electrons and holes exist on different sides of the heterojunction, thus separating electrons and holes. This reduces radiative recombination due to reduced spatial overlap of the electron and hole wave functions, with a subsequent increase in the exciton lifetime [18]. Figure 9 (previous page) shows an example of a type-I (on the left) and a type-II (on the right) band alignment from two different material systems.

### 2.2 The Efficiency Limit of Solar Cells

The efficiency of a solar cell, η, is one of the commonly used criteria when comparing devices to each other [11]; it is defined as the ratio of power density, $J_m \bullet V_m$, to incident light power, $P_s$.

$$\eta = \frac{\boldsymbol{J_m * V_m}}{\boldsymbol{P_s}} \quad \textbf{(1)}$$

$P_s$, itself is related to the irradiance of the Sun and is a function of many different variables including climatic conditions and atmospheric attenuation. As an approximation, the Sun itself can be thought of as a black body, or a body capable of absorbing all incident electromagnetic radiation and thus, has a spectrum in accordance to Planck's Law. Experimental data indicates that the Sun has roughly a 5760 K

effective temperature; based on Planck's law, the irradiance per wavelength can be plotted [11].

More accurately though considering other variables, such as: atmosphere attenuation, the irradiance from the Sun is lower. The reduction is dependent on the amount of atmosphere traveled through and, of course, also varies based on season and other factors. This attenuation is calculated by an Air Mass (AM) factor, n, and is a function of $\gamma_s$, the angle of elevation of the Sun [11].

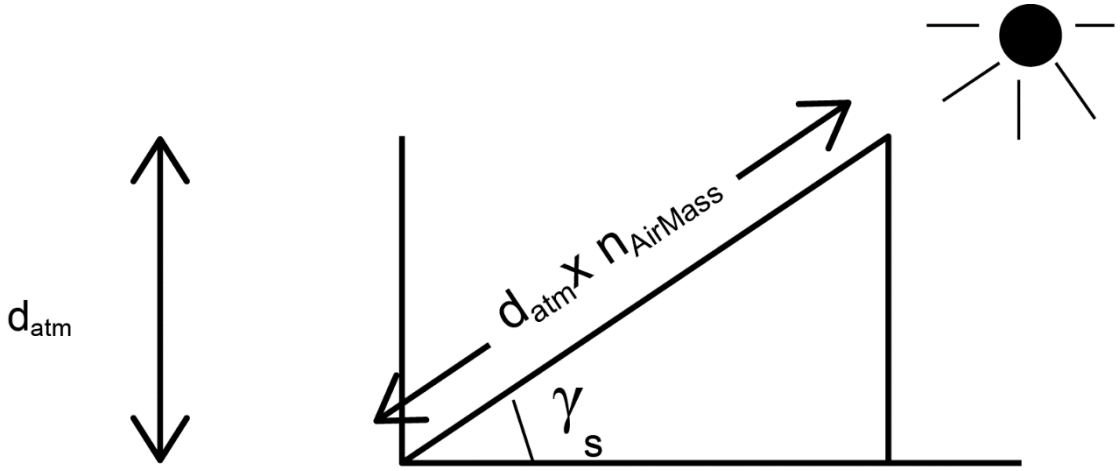



**Figure 10. Optical Depth of the Atmosphere**
In this figure, $\gamma_s$ represents the angle of elevation of the Sun while $d_{atm}$ represents its height. $N_{airmass}$ represents an air mass factor.
*J. Nelson, The physics of solar cells. London: Imperial College Press, 2003.*

$$n_{airmass} = \frac{1}{\sin\gamma_s} \quad \textbf{(2)}$$

The standard the solar cell industry adheres to is called AM1.5, which is the equivalent to the Sun being 42° above the surface. For comparison, these spectrums, along with AM1.0, the extraterrestrial spectrum, are shown in Figure 11 [11].

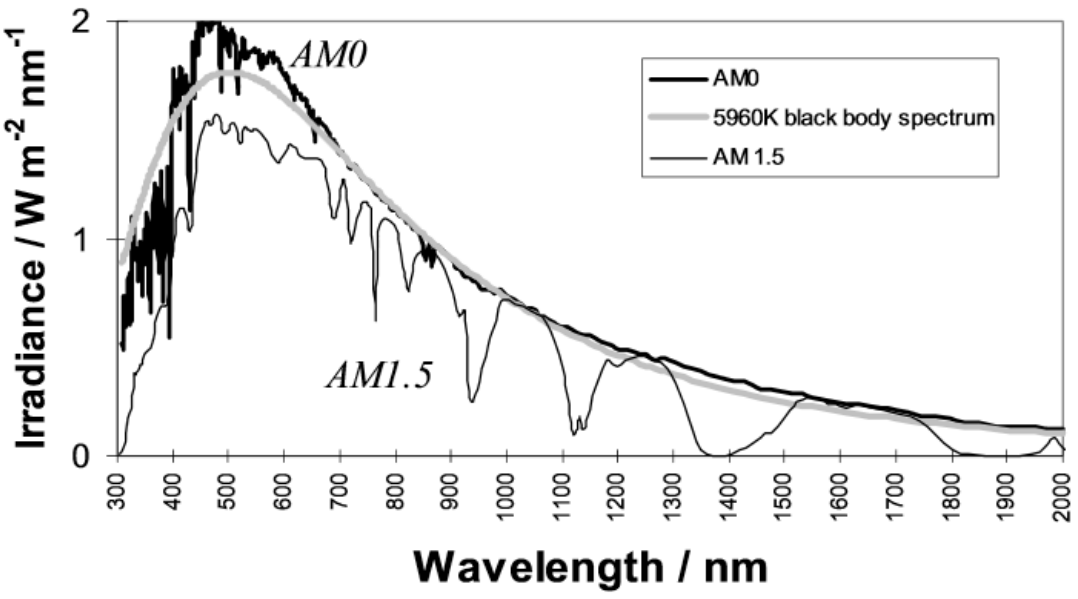



**Figure 11. Solar Spectrum**
Experimental spectrums of the Sun on Earth (AM 1.5), extraterrestrial spectrum (AM 0) and black body spectrum (5760 K) plotted against wavelength in nm. The 5960K as it appears in the figure is a typo.
*J. Nelson, The physics of solar cells. London: Imperial College Press, 2003.*

Every process involved in the energy conversion of light to electricity both outside and inside the cell does not perform in a perfect manner. Just how much energy is lost varies with materials used, temperature, and other practical effects for commercial cells such as weather. Some of these losses are avoidable, but others are inevitable. The list of inescapable losses and how it affects performance on a cell, was calculated in the aforementioned Shockley-Queisser limit; named after the scientists who calculated it in their famous detailed balance paper in 1961 [16].

The formulation for the Shockley-Queisser limit involves several considerations, as well as, assumptions of intrinsic losses in a single p-n junction solar cell.

Recombination, a process “opposite” of absorption, was assumed to be radiative, meaning electrons, if not extracted, drop back directly to the valence band emitting a photon in the process. The next loss taken into account was the band gap of the device itself and with that, an assumption of a step-like absorption in that photons above the band gap were absorbed and below the band gap none were. The last consideration was that both the cell and Sun emit black body radiation. Lastly, some non-intrinsic effects that can affect real cells were not studied here. These include the effects of reflection on the surface of the cell, contact resistance, and the mobility of carriers. The results of this study shown below in Figure 12, also includes the Semi-Empirical Limit and the best experimental silicon cell at the time [16].

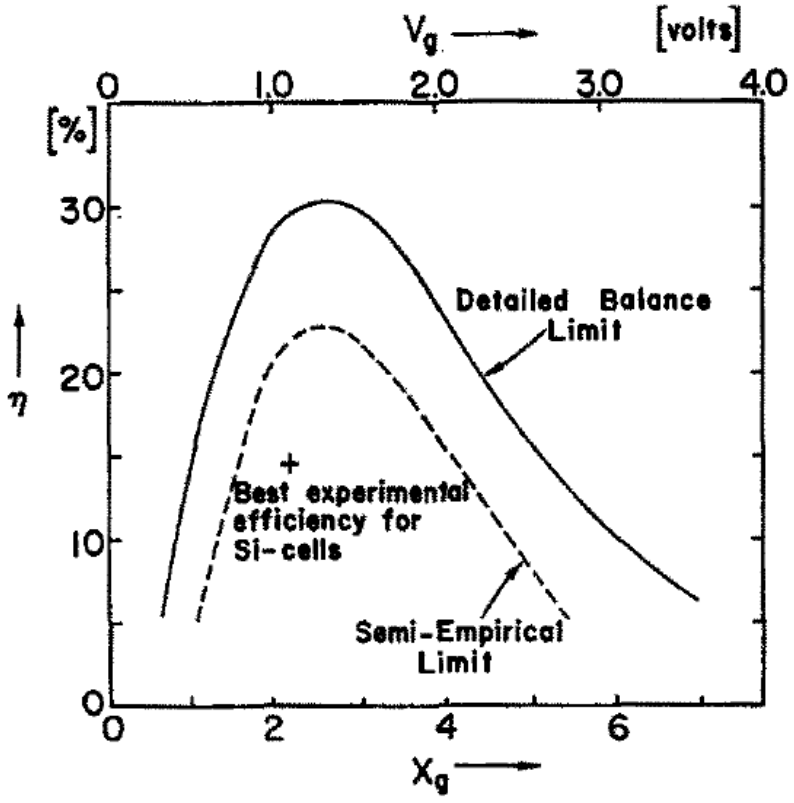



**Figure 12. Shockley Queisser limit and Semi-Empirical Limit**
$V_g$ refers to the band gap while $X_g$ refers to a ratio of the band gap to $k_bT$.
*W. Shockley and H. Queisser, "Detailed Balance Limit of Efficiency of p-n Junction Solar Cells", J. Appl. Phys., vol. 32, no. 3, p. 510, 1961.*

It should also be noted that this theoretical calculation has been revisited by several researchers. One approach taken by Hirst and Ekins-Daukes [19] takes the losses already considered by Shockley and Queisser and reexamines them while also investigating new losses.

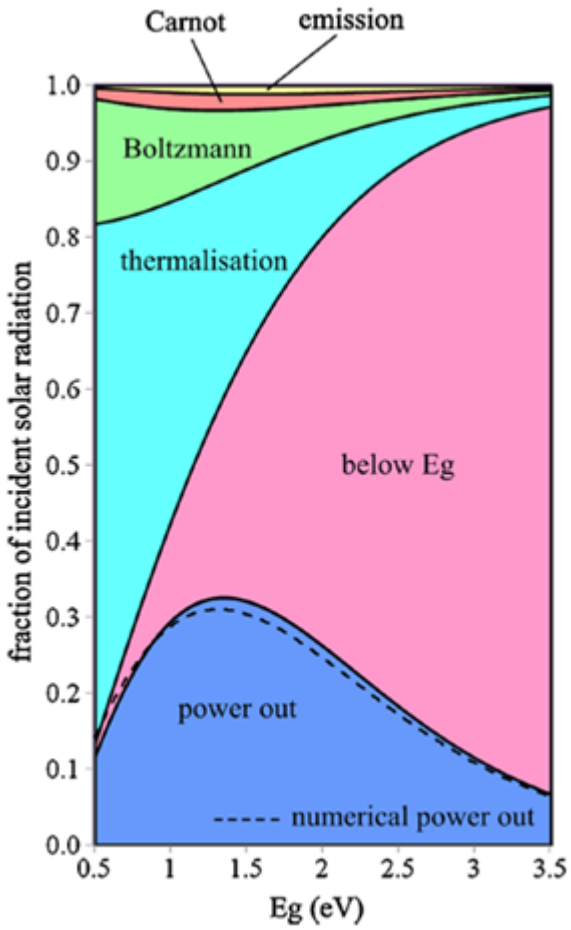



**Figure 13. Intrinsic Losses in a Solar Cell as a Function of Band Gap**
Shockley-Queisser limit (blue) plotted with below band gap, thermalization, Boltzmann, Carnot and emission losses as a function of band gap.
L. Hirst and N. Ekins-Daukes, "Fundamental losses in solar cells", Prog. Photovolt: Res. Appl., vol. 19, no. 3, pp. 286-293, 2010.

In all, they study five fundamental losses. The first loss is the below band gap loss, or spectral loss, and it represents the largest loss of efficiency of a solar cell. The second loss, thermalization, is a process where high energy carriers generated by high

energy photons above the band gap lose that additional energy as heat - or via phonons - if not immediately extracted through contacts. The next highest loss considered is the Boltzmann loss. This is a result of different étendue, a term referring to the solid angle of the source and the area of incidence of light, between absorption and emission of photons by the cell that results in increased entropy. Another loss considered is a Fermi Level loss also known as the Carnot factor. The Fermi level loss is a result in the increase of entropy of carriers in the system due to a non-zero temperature resulting in additional energy needed for the conversion of energy. This effect is not large due to the temperature difference between the Sun and the cell, but it exists nonetheless. Lastly, the emission loss due to recombination is considered [19]. The impact of these losses on efficiency is plotted per band gap (in pink, light blue, green, red and yellow for each different loss) above the Shockley-Queisser limit shown in blue in Figure 13 on the previous page. The visualization of the mechanisms of some of these losses are shown in Figure 14.

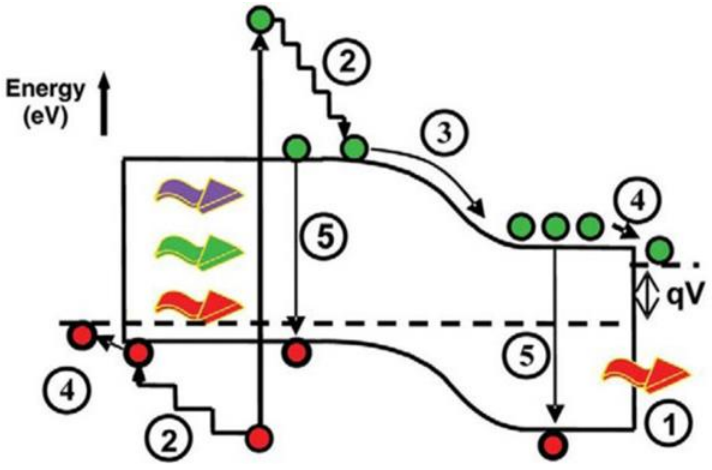



**Figure 14. Loss Processes in a Standard Solar Cell**
(1) Below band gap absorption. (2) Thermilization. (3) Junction (4) contact voltage losses. (5) Radiative recombination
*G. Conibeer, "Third-generation photovoltaics", Materials Today, vol. 10, no. 11, pp. 42-50, 2007.*

### 2.3 Methods to Exceed the Shockley-Queisser Limit

Several approaches within third generation research have been considered over the years to achieve higher efficiency cells by circumventing the loss mechanisms imposed by the theoretical limits detailed by Shockley and Queisser and shown in Figure 12 and their processes involved in Figure 13. One such approach is saving energy lost due to absorption of photons above the band gap. One way this can be done is through multiple exciton generation (MEG), which refers to either multiple photons generating a single exciton (electron-hole pair) or a high-energy photon degrading into several excitons. Although not entirely understood, this process has been observed to be more efficient in quantum dots [17]. This approach has a theoretical limit that depends on the highest energy photons above the band gap that can be absorbed. At 3 times the band gap, the theoretical efficiency would be 42% [17].

Another way to save energy lost related to the absorption of photons would be to use an up and down converters with a solar cell. These converters could either reduce the energy of a high energy photon (convert from UV to visible) or increase the energy of an incoming photon (convert from IR to visible) [17]. Similarly to the MEG method, this results in less wasted incoming energy related to a single a band gap. Due to the spectrum having a high energy tail, an up converter results in a higher theoretical efficiency than a down converter at 48% under one Sun. Currently, both devices have not reached high efficiencies, but are still being researched [15] [17].

Another loss with solar cells that can be prevented is thermalization [19]. The concept, known as a hot carrier cell, involves a strategy to prevent energy loss of high-energy (hot) carriers before they lose their energy to phonon interactions within the

lattice, which enables these cells to potentially achieve higher voltages across the device. Cells designed for this role require an absorber material designed to slow the rate at which the carriers cool and also require contacts designed specifically for the higher energy carriers so that they may be extracted selectively. Both of these requirements are challenging, however, in spite of this, hot carrier cells hold promise and have been theorized to achieve a high efficiency of 65% under 1-Sun illumination [15] [17] [20] [21].

A more mature technology to achieve efficiencies higher than the previously calculated detailed balance limit are cells created with multiple p-n junctions. Multiple junctions create the same desired effect of utilizing a larger energy range of photons as other third generation photovoltaics, but this is accomplished through the use of multiple materials in tandem with each other. Different materials with varying band gaps are selected and then stacked together. Each additional junction stacked, utilizes more of the spectrum, but in doing so, increases both cost and thickness of the device. Because of the complexity and cost, these cells are used in concentrated sun systems to increase their efficiency per watt generated. In addition to the high efficiency III-V single crystalline structures ideally used, several other materials including different thin film technologies as well as amorphous silicon and silicon nanostructures are being considered to help lower cost [17]. Lastly, with an infinite amount of energy levels, these cells can perform with an efficiency of 86.6%, with losses only due to the unavoidable thermodynamic effects [15] [17].

# Chapter 3: Intermediate Band Solar Cells

## 3.1 Concept

Intermediate band solar cells (IBSCs) are another idea that can take advantage of a larger range of photon absorption, but are different from multi junction cells in that they still only have a single p-n junction, but use an “intermediate band” of lower energy states (a mid-gap band) introduced in between the valence band and conduction band. This intermediate band is illustrated in Figure 15 (next page) along with the accompanying band diagram. The operation and absorption is this system works similarly to a conventional solar cell, but now accepts lower photon energies, increasing the current harnessed. Carriers can now be excited from the VB to IB and then IB to CB in addition to the traditional VB to CB. In other words, it creates a two photon absorption process. Carriers excited to the IB are confined to those states until another photon excites that carrier out of the barrier. Thus, this new band also has a quasi-Fermi level associated with it just as with the CB and VB [15] [17] [22] [23] [24] [25]. And, since the voltage is determined by the difference of electron and hole quasi-Fermi levels, the overall band gap still is maintained so long as the IB continues to be isolated [15] [22] [23] [24] [25]. This entire process leads to an increased flow of carriers with no loss of voltage. These cells have the potential for 63.2% efficiency under full concentration [15] [17] [22] [24] [25].

## 3.2 Creating an Intermediate Band

Numerous methods can be used to create IBSCs including impurities [15] [17]. Normally, impurities in devices can introduce defects which, under normal conditions, interrupt the operation of a device by introducing states that can decrease the open

circuit voltage due to the prevalence of non-radiative centers and an increased dark current. However, intentionally introducing defects can create an intermediate state if done correctly [15] [17] [22] [26].

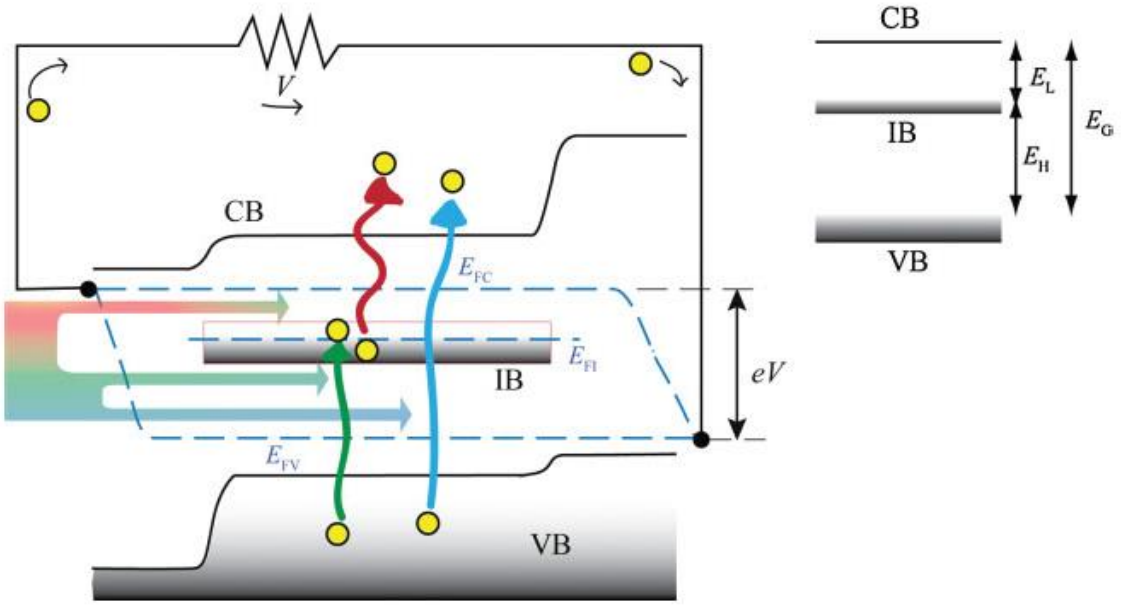



**Figure 15. Intermediate Band Solar Cell Band Diagram**
Left figure: A third band is inserted into a traditional solar cell band diagram. Results in $E_G$ being split into $E_L$ and $E_H$ for the IB to CB transition and VB to IB transition respectively. Photons of those energies now can be absorbed by the cell through two photon absorption shown here with a green and red photon. Of course, the cell still absorbs high energy photons shown here in blue. A third Fermi level exists due to the IB and at equilibrium, lies in the middle of the IB. Right figure: A simplified view of the three bands and the different energies associated with transitions between them.
*A. Luque and A. MartÃ-, "The Intermediate Band Solar Cell: Progress Toward the Realization of an Attractive Concept", Adv. Mater., vol. 22, no. 2, pp. 160-174, 2010.*

It has been shown in multiple material systems thus far that it is possible to get a response below the band gap in quantum efficiency measurements similarly to an IB cell. Preservation of voltage and an increase in current has also been shown in different devices using this method. Sub band gap absorption has been observed in some material systems and photoluminescence/photoreflectance also supports the idea that an IB has been made in other systems utilizing this method [24].

A system with highly mismatched alloys also can create an intermediate band [26]. These systems work by creating a third band from either the valence band or conduction band depending on the material used [26]. As with intentionally introduced impurities, these systems have shown both a sub band gap QE response, as well as, sub band gap absorption. An increase in short circuit current has also been noted along with evidence of an IB from PL/PR measurements. Also, unlike an impurity derived IB, two photon sub band gap photo current has been observed and electroluminescence also shows evidence of an IB transition. Unfortunately, voltage preservation has not yet been shown in these types of devices [24].

Another way to create an IB is with quantum dots due to an interesting property: their ability to confine particles in three spatial dimensions. Quantum dots (QDs) work similarly to quantum well structures with the difference being that quantum wells confine particles in, only, *one* dimension; thus, QDs are the zero dimensional analog of a quantum well. This confinement forces the carriers to transition similarly to how an atom operates when you excite electrons; i.e., they no longer have a continuum of energy states possible but, must adhere to discrete, quantized, energy levels. Because of this, they are sometimes termed “artificial atoms”. These “artificial atoms” have the additional benefit of being “tunable” in the sense that changing the size of the QD, also adjusts the discrete energy levels that carriers can exist at [27]. This variability in the nature of the QD has made it of great interest to semiconductor physics in general, as well as, being able to create a proper IB of suitable energy. This led to QDs being the first system implemented for IBSCs. Since then, they have also been the most studied and are the most mature IB technology available [23] [28] [29] [30] [31] [32].

Among the QD systems available, the most studied is the InAs/GaAs material system [23] [25] [28] [29] [33]. However, there are several drawbacks associated with this system [34]: poor spectral overlap, large recombination losses, and others, such as, thermal coupling of the CB to the QD energy levels which reduces $V_{oc}$ [32]. InAs/GaAsSb is a promising alternative QD system for IBSCs because GaAsSb acts as a strain-reducing layer on InAs QDs, which is important since strain can induce defects; that ultimately reduce short-circuit current density and aid in the collapse of $V_{oc}$ [32] [35] [36] [37]. Also, this material system improves the QD uniformity and density to $4x10^{11}$ $cm^2$ [34]. Moreover, this system has been experimentally shown to have all processes key to IB systems [24]. InAs QDs and their behavior within a GaAsSb matrix are the subject of this thesis.

# Chapter 4: Investigation into Four InAs/GaAsSb Devices

## 4.1 Characterization of Solar Cells

### *Photoluminescence Spectroscopy*

There are several experiments used to characterize solar cells with each giving a different insight into the material structure, function of the device, and how different aspects perform. Photoluminescence (PL) measurements are a common technique for semiconductor analysis. It is a non-destructive measurement that does not require a wired device. PL measurements are performed by excitation of a laser of the sample with an energy above the sample's band gap. This excites carriers which then relax to the band gap minimum. After some time elapses these carriers recombine, since there is no method of extraction; in the process of recombining, they emit a photon of the same energy as the band gap. The photons emitted by the sample are measured by a detector and recorded [38].

PL measurements are used to determine recombination paths within samples; when paired with the external quantum efficiency (*EQE*) (which is discussed in the following section) a complete understanding of what is happening with carriers within the sample is developed: whether they are recombining or being extracted at different wavelengths and at different temperatures by means of temperature and power dependent measurements. Typically, PL measurements result in peaks indicative of the materials present in the sample, though may also show the presence of defects. Depending on the shape of these peaks, it can give information about the variance in the different bands present in the material. Temperature dependent PL (TD PL), then,

presents data about how these bands change with temperature and if this change is the result of thermal expansion or if something more is happening within the sample [39].

Power dependent photoluminescence (PD PL) measurements are another type of PL measurement. In this experiment, the power of the emission source of photons is varied with neutral density filters. These measurements can be used to evaluate the band alignment in the system by noting if peak energy depends on power of the source. As previously shown, varying the amount of antimony in the system shows a shift from type-I band alignment to type-II [34] [35] [41]. Whether or not the system is type-I or type-II helps in determining carrier transport through the system.

### *External Quantum Efficiency*

External quantum efficiency (EQE) measurements are useful in describing device characteristics of samples. EQE curves are generated from shining a focused light source at individual wavelengths onto a sample and getting a ratio of carriers extracted to the number of photons incident on the sample by the light source. An identical measurement on a known response from a detector is then conducted [11].

Since this is a per wavelength measurement, the EQE curve gives information about how much, or which materials in the sample are contributing to current generation and the band gaps of each material. The data also provides information about total short circuit current density ($J_{sc}$) for the sample since EQE is not dependent on the incident spectrum, but is dependent on the variables that $J_{sc}$ is dependent on; such as: charge separation, efficiency of charge collection, and the absorption coefficient of the solar cell material. As such, $J_{sc}$ is a function of EQE by:

$$J_{sc} = q \int_{E_1}^{E_2} b_s(E) QE(E) dE \quad \textbf{(3)}$$

where $q$ is the charge of an electron, $b_s$(E) is the incident spectral photon flux density, and QE(E) is the probability that an incident photon delivers one electron to the circuit [11].

The shape of an EQE measurement is associated with each region (front/back surface) and represents crucial information regarding recombination in those regions of the device as well. This data can then be paired with photoluminescence information to give a more complete understanding of carrier extraction versus carrier recombination processes and which one dominates. Temperature dependent EQE adds another layer of understanding by providing clues as to how thermal assistance can influence carrier extraction processes.

*Current-Voltage Analysis*

Current-Voltage (IV) curves are immensely effective in determining different electrical properties of a diode. Since a solar cell is a diode in the dark due to its similar makeup and p-n junction, a relationship between bias and the resulting current can be established similarly to how it is done with a diode. Thus, an understanding of the complex behavior of these devices starts with the Shockley diode equation; which is the most general model for diodes in that it assumes, based on its derivation, that the only mechanisms that generate current are diffusion of carriers and drift from the electric field created by the p-n junction [11].

$$J_{dark}(V) = J_0\left(e^{\frac{qV}{K_BT}} - 1\right) \quad \textbf{(4)}$$

$J_{dark}$, the current density in the dark, is a function of $J_0$, the dark saturation current density, $q$, the charge of an electron, $k_B$, Boltzmann's constant, $T$, the temperature, as well as, $V$, the applied bias. Since solar cells are minority carrier diffusion devices, the light generated current opposes the dark current; so, in the light the total current density becomes

$$J(V) = J_{sc} - J_{dark}(V) \quad \textbf{(5)}$$

More realistically, though, cells have parasitic resistances that affect carrier flow through the device. These are the series resistance, $R_s$, which is the resistance of the contacts and then also the shunt resistance, $R_{sh}$, which can provide an alternate route to the main junction. Additionally, few solar cells are "ideal" in that recombination becomes a factor that must be considered. This factor is referred to as the ideality factor, $n$, and for devices with recombination, is set at 2 [11].

$$J(V) = J_{sc} - J_0\left(e^{\frac{q(V+JR_S)}{nK_BT}} - 1\right) - \frac{V + JR_S}{R_{SH}} \quad \textbf{(6)}$$

The solar cells tested here are further complicated due to additional carrier paths afforded by the material system. Thus, we have considered an additional (tunneling) diode and a non-ohmic (SCLC) leakage current for our system, as proposed by Williams *et al*. for non-ideal CIGS-based solar cells [42]. The equation used is of the following form and considers only the dark current density ($J_D$):

$$J_D(V) = J_{01}\left(e^{A_1(V-J_DR_S)} - 1\right) + J_{02}\left(e^{A_2(V-J_DR_S)} - 1\right) + \frac{V - J_DR_S}{R_{SH}} + k(V - J_DR_s)^m \quad \textbf{(7)}$$

Here, $A = \frac{q}{nK_BT}$ and $n$ is allowed to vary hence $A_1$ and $A_2$. $k$ is a coefficient related to the length and conductivity of the current path and $m$ is a power factor that is higher than 2 in our system since a high density of deep traps are present. $J_{01}$ represents the main junction diode while $J_{02}$ represents the tunneling diode. The third term represents the current due to ohmic shunt resistance while the last term represents a non-ohmic (SCLC) leakage current [42]. This equation represents the equivalent circuit shown in Figure 16.

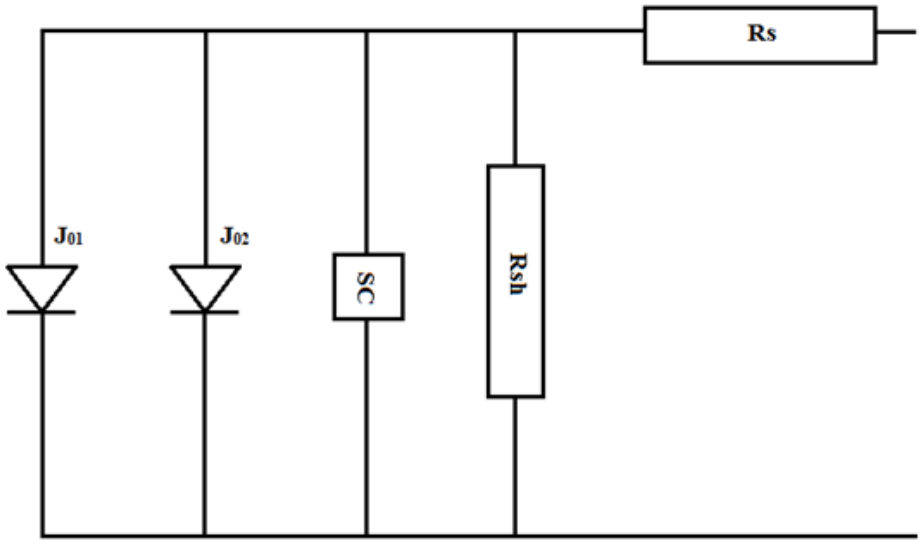



**Figure 16. Equivalent Circuit of Model**
Multiple current paths of carriers represented by diodes $J_{01}$ and $J_{02}$, a non-Ohmic space charge leakage current (SC) and an Ohmic leakage current $R_{SH}$. $R_S$ represents the series resistance.
Williams, *Benjamin L. et al. "Identifying Parasitic Current Pathways In CIGS Solar Cells By Modelling Dark J-V Response". Prog. Photovolt: Res. Appl. 23.11 (2015): 1516-1525. Web. 5 Apr. 2016.*

The use of this equation as a model affords the extraction of parameters $J_{001}$ and $J_{002}$ (equations 8 and 9); along with the activation energy, $\Delta E$, of the recombination and

diffusion process, which should be close to the band gap; as well as, the barrier height of the tunneling diode, *B*, via the following equations [42]:

$$J_{01} = J_{001}T^2 e^{\frac{-\Delta E}{nK_BT}} \quad \textbf{(8)}$$

$$J_{02} = J_{002}e^{BT} \quad \textbf{(9)}$$

All of these parameters, together, in combination with the other experiments, temperature dependent photoluminescence (PL), and temperature dependent external quantum efficiency (EQE), afford a thorough understanding of the nature of the several mechanisms contributing to the overall performance of the systems being studied here.

## 4.2 Experimental Design and Setup

### *Sample Growth*

This study was conducted on a series of 4 different QD samples grown by molecular beam epitaxy (MBE). 550 nm of n doped GaAs layer serves as the buffer layer grown on top of the substrate. In the middle of the doped GaAs (250 nm) is a 30 nm layer of $Al_{.30}Ga_{.70}As$. After the doped GaAs, a 50 nm layer of intrinsic GaAs was grown. The $InAs/GaAs_{.86}Sb_{.14}$ QD/matrix was grown next and is where the control sample and quantum dot samples vary. For each of the dot samples, 20 nm of $GaAs_{.86}Sb_{.14}$ was grown followed by 3 monolayers of InAs (QDs); 3 monolayers was chosen based on previous PL data that gave evidence that this thickness had the brightest PL [34]. This was then repeated 3, 5, or 7 times for the 3, 5, or 7 layer samples, respectively. For the control sample, no QDs were grown within the

$GaAs_{.86}Sb_{.14}$ matrix of equal thickness. All 4 samples are then capped by 30 nm of $GaAs_{.86}Sb_{.14}$. The sample is finished with another 50 nm of intrinsic GaAs and then p doped GaAs (450 nm) with another 30 nm $Al_{.75}Ga_{.25}As$ in the middle (at 200 nm) of the p doped GaAs. Thus, a p-i-n structure was developed with GaAs serving as the p-n diode with the InAs/$GaAs_{.86}Sb_{.14}$ QD/matrix serving as the intrinsic region for the layered samples and $GaAs_{.86}Sb_{.14}$ serving as the intrinsic region for the control sample.

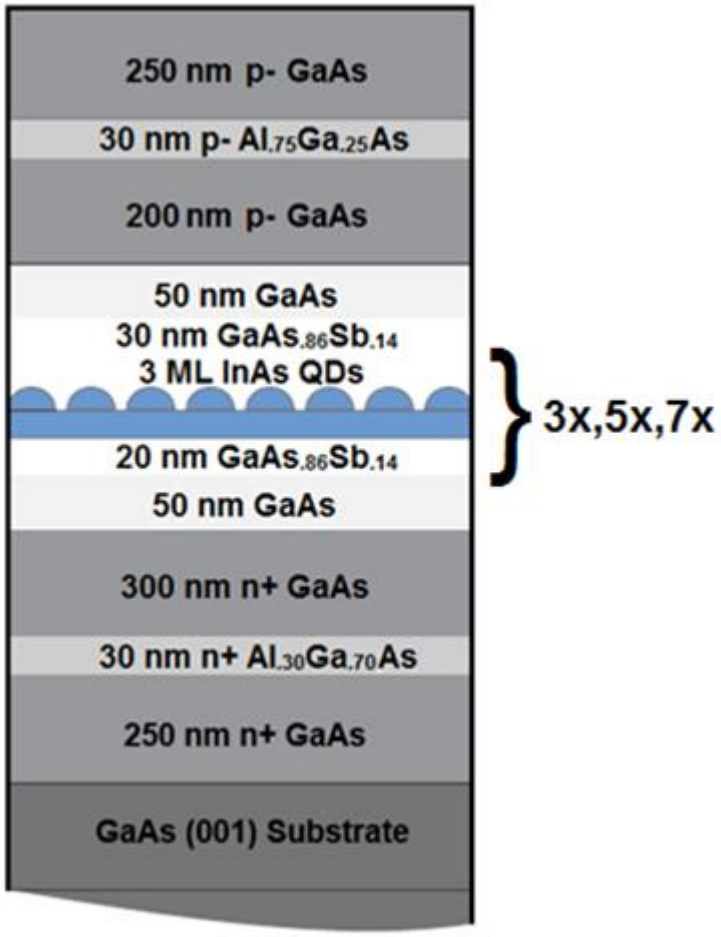



**Figure 17. Device Structure for a Sample Containing One Layer of QDs**
Layers of the devices. The GaAsSb and QDs are repeated 3, 5, and 7 times in the QD samples and the control sample only has GaAsSb.

*Sample Preparation*

Because IV and EQE measurements require applying a bias, the samples needed an electrical connection and so they were processed into devices using Au/Zn/Au and InGe/Au metals for p-type and n-type contacts, respectively. The samples, two at a time (5 and 7 layer; then, 3 layer and control), were then mounted onto two copper plates with conducting Epo-Tek epoxy. Bonding pads were then mounted onto the copper plates with non-conducting Epo-Tek epoxy. The samples were then baked at 100 °C for two hours to let the conducting and non-conducting epoxy cure. Lastly, gold nanowires were then connected from the samples to the bonding pads manually using indium. Two of the final solar cells are shown in Figure 18.

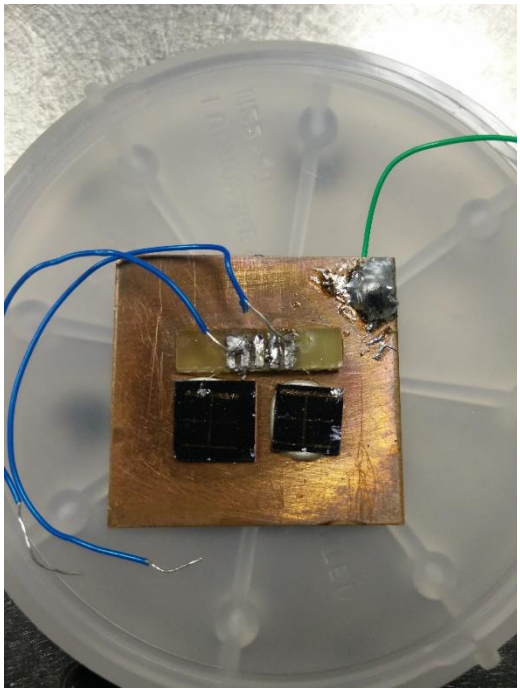


**Figure 18. Two of the Solar Cell Samples**
The devices here have already been mounted and wire bonded. They were grown at the University of Oklahoma by MBE and processed at the University College of London.

*IV Measurement Experimental Setup*

The samples were inserted into a Linkam micro cryostat where they were connected via 24 American wire gauge (AWG) wires from the bonding pads to the cryostat. The cryostat itself was connected to a Liquid Nitrogen dewar with a pumping station and temperature controller, as well as, electrically connected to a Keithley 2400 source meter controlled by the computer software: Oriel IV Test Station. A Logitech webcam took video which was used to determine dark current since the dark currents for the samples were an order of magnitude lower than what was recorded by the computer software. The cryostat was placed under a Newport Oriel Sol 2A solar simulator so light IV measurements could be done in the same temperature study as dark IV measurements. A reference cell was used in conjunction with the lamp to determine the amount of Sun being applied to each sample. Any excess ambient light was eliminated.

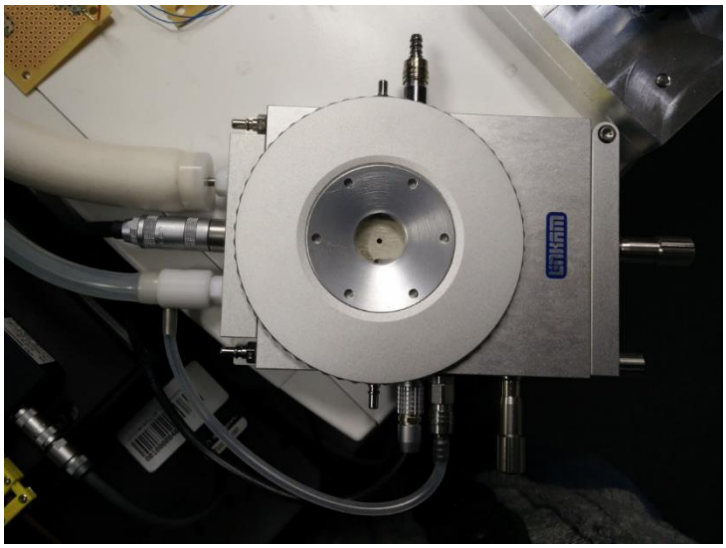


**Figure 19. Linkam Micro Cryostat**
Cryostat plus various connections to the temperature controller and dewar (lower and upper left), Keithley, left, and port for purging on top.

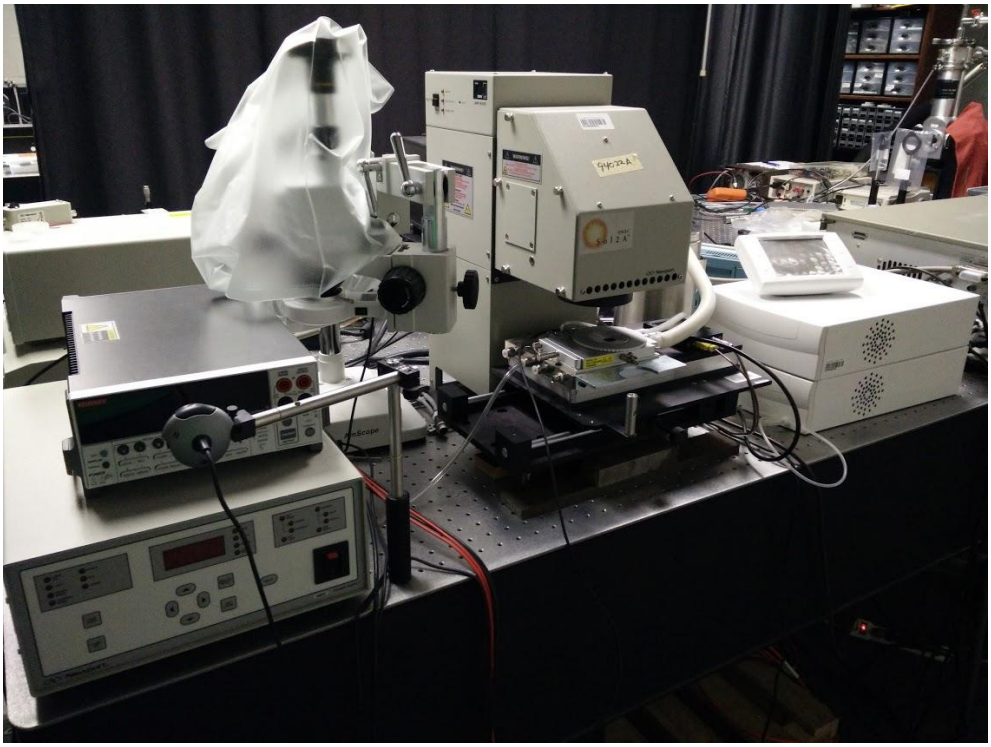


**Figure 20. IV Experimental Setup**
Includes Keithley (upper left), voltage source (lower left), solar simulator with micro cryostat (middle), temperature controller (right).

Once each sample was in place, the cryostat was sealed and prepared for a decrease in temperature. This was done by first purging the air inside the cryostat for five minutes. The sample was then cooled down to 77 K from room temperature in 10-15 minutes. At each temperature, all measurements for that temperature were carried out in roughly 7 minutes before going to the next temperature. These temperatures ranged from 77 K to 350 K in increments of 10 K, except for the first to second temperature, which went from 77 K to 80 K.

The conditions for the measurements all had the same bias of -1.5 V to 1.5 V in .05 V steps applied, but varied in the amount of light (with use of a filter) from the solar simulator that excited the sample so as to extract different information from each measurement. The solar simulator was turned off for the dark IV measurements. In

addition, the window to the cryostat was blocked as well to prevent any possible ambient light from hitting the sample. To obtain information about the quantum dots, only a partial amount of light was let through for a filter IV measurement at each temperature. This was accomplished with a long pass 870 nm GaAs filter that was placed on the window to the cryostat. Lastly, light IV measurements were conducted with the solar simulator's unfiltered light hitting the sample. It should be noted that the window of the cryostat does slightly reduce the amount of light reaching the sample in all experiments.

### *EQE Measurement Experimental Setup*

The Linkam cryostat and accompanying Linkam temperature controller and dewar utilized in the IV measurements were employed for these experiments as well. An Oriel 300-watt xenon arc lamp served as the light source. The light was then passed through an Oriel Cornerstone 260 monochromator for measuring the response of the sample to a varying single wavelength of light. Two lenses by Newport, a Borosilicate Crown collimating and focusing lens, as well as, a Newport Borofloat 33 flat mirror were used to focus and reflect the resulting light onto the sample and detector. In the case of the sample, the resulting light was reflected at 45 degrees downward since the cryostat could not be held vertically. To create a similar situation and since the light could not be focused downward on the detector, it instead was reflected at 45 degrees to the left of the rail system holding the lenses. A Newport power meter (Model 1936-C) was connected to the cryostat and measured the response of the sample and detectors. Oriel TracQ Basic software was used to collect data.

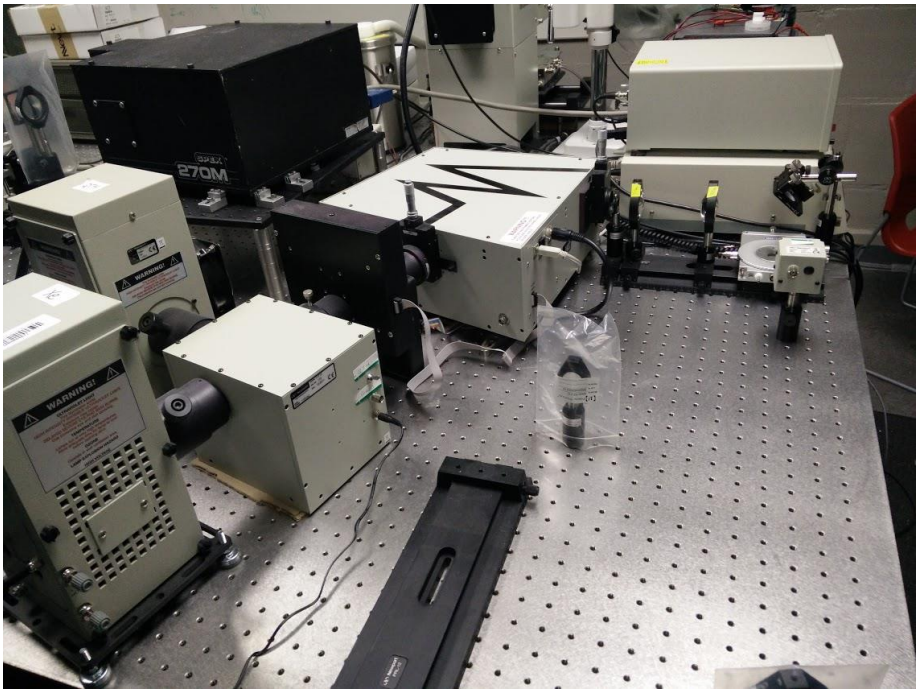



**Figure 21. EQE Experimental Setup**
Lamps (left, monochromator (middle), lens setup, detector, micro cryostat (right)

Since the measurement range of 400 nm to 1300 nm was broad, two detectors instead of one were needed to match the sample data against. A Newport model 71650 continuous silicon detector (suitable for 400-1100 nm) as well as a Newport model 71653 continuous germanium detector (suitable for 700-1800 nm) and their associated response files were used for this purpose.

The detector measurement was recorded and saved first. This file was used as the reference measurement for all samples. Measurements for each sample were then conducted similarly to the IV measurements in that the same temperature range and the same increments of temperature were used. The same procedure of purging for five minutes and then cooling down to 77 K in roughly 10-15 minutes was followed. To balance resolution and time, 3 nanometer steps were picked for the measurements. With this choice of step size, each temperature took 10 minutes instead of 7 minutes for IV

measurements. The additional time made condensation an issue on the outer body of the cryostat and so $N_2$ gas was passed through the body as a way to alleviate this. All measurements were done in an analogous environment to the IV measurements with the addition of a zeroing out setting on the power meter.

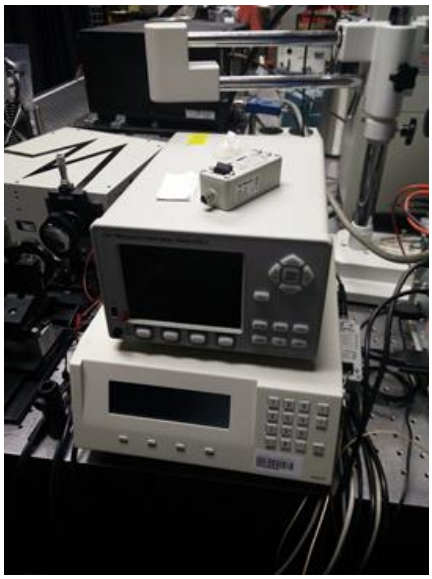


**Figure 22. Continuous EQE Meter**
Continuous EQE power meter (top).

*PL Measurement Experimental Setup*

A HeNe laser (632.8 nm) was used as the excitation source in conjunction with various Borosilicate Crown Newport lenses and Borofloat 33 flat mirrors to focus the light on the sample. A neutral density filter wheel placed in front of the laser was also used for PD PL. A closed-cycle He cryostat system was used via a temperature controller to adjust the temperature. Emission from the sample was focused using a rail rider setup similar to the EQE measurements, with two other Newport lenses. A linear InGaAs array multi-channeled detector was used to collect the data, which was cooled using liquid nitrogen. This data was recorded using the Winspec software. Data for all

samples was taken over a broad range of 750-1500 nm taken over several 100 nm windows with 15 nm overlap and then stitched together also using the Winspec software.

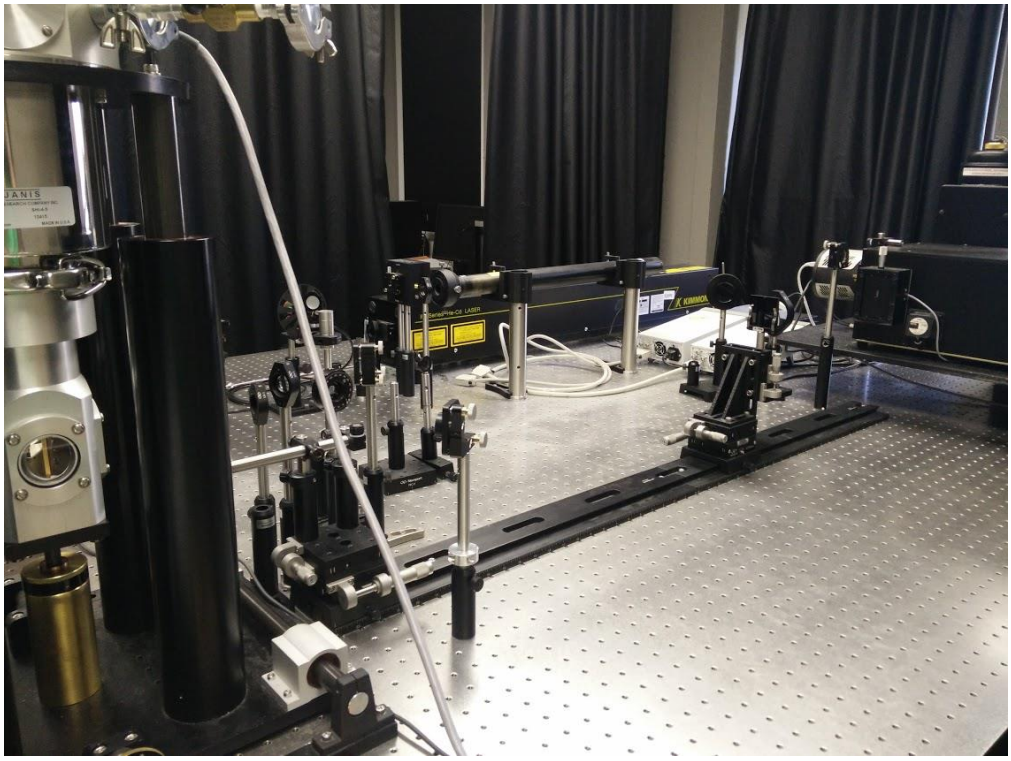


**Figure 23. PL Experimental Setup**
Laser (far middle), cryostat/sample holder (left), rails and filter holder (middle), detector (right)

The sample was first placed into a closed-cycle He cryostat system and then the vacuum was pumped down to roughly $10^{-6}$ torr with a turbo molecular pump. The temperature was then dropped to 4.2 K using the closed cycle He compressor. The vacuum pump was then turned off as the system was cryo-pumping after that. While the temperature was dropping, the detector was cooled as well.

PD PL was performed first at 4.2 K after focusing the light and adjusting slit width to maximize resolution around the dot peak at roughly 1060 nm. A filter wheel housing different strength neutral density filters was placed in front of the HeNe laser

and rotated for each measurement. TD PL was done next for 4.2 K, 7 K, 10 K, and then in 5 K intervals up to 75 K. 77 K to 350 K was ran similarly to IV/EQE measurements, though each measurement lasted about 4 minutes per temperature. At a certain temperature (200 K for the samples with QD and 77 K for the control sample), the counts were increased with an increase in slit width and time the shutter was open, since the PL signal had quenched by those temperatures. The PD PL also saw a rapid decrease in signal with increasing filter strength and therefore reduced excitation intensity; counts were also similarly increased during these measurements as well. The increase multiplier for the counts was noted for future comparison of data.

## 4.3 Experimental Results and Discussion

*Low-temperature Photoluminescence*

Figure 24 (a) shows a normalized intensity PL plot at 4.2 K. Generally for PL, the lowest energy transition is the brightest [38] and this appears to be true in all the samples here. The control sample has two main transitions – ~830 nm corresponding to PL from GaAs and then ~875 nm which is a result of GaAsSb PL and related complexes. There is also some low energy PL in the control despite absence of QDs. This is made more evident in the inset which shows a log plot of the normalized intensity. This is a result of defects present in the material in that region due to the known large lattice mismatch of 10% between GaAs and GaAsSb [40]. The fact that defects do not show a shift with temperature typical of Varshni-type expansion [39] agrees with this hypothesis as well. The inset also highlights a small amount of PL at ~ 910 nm just after the GaAsSb peak due to inhomogeneity in GaAsSb. Lastly, the two peaks in the control sample are not broad, which means that the defects that are present

seem to have no effect on the quality of the PL at those energies, though there may be some inhomogeneity in the material as there is some surface recombination on the high energy side of the GaAs peak due to the slope.

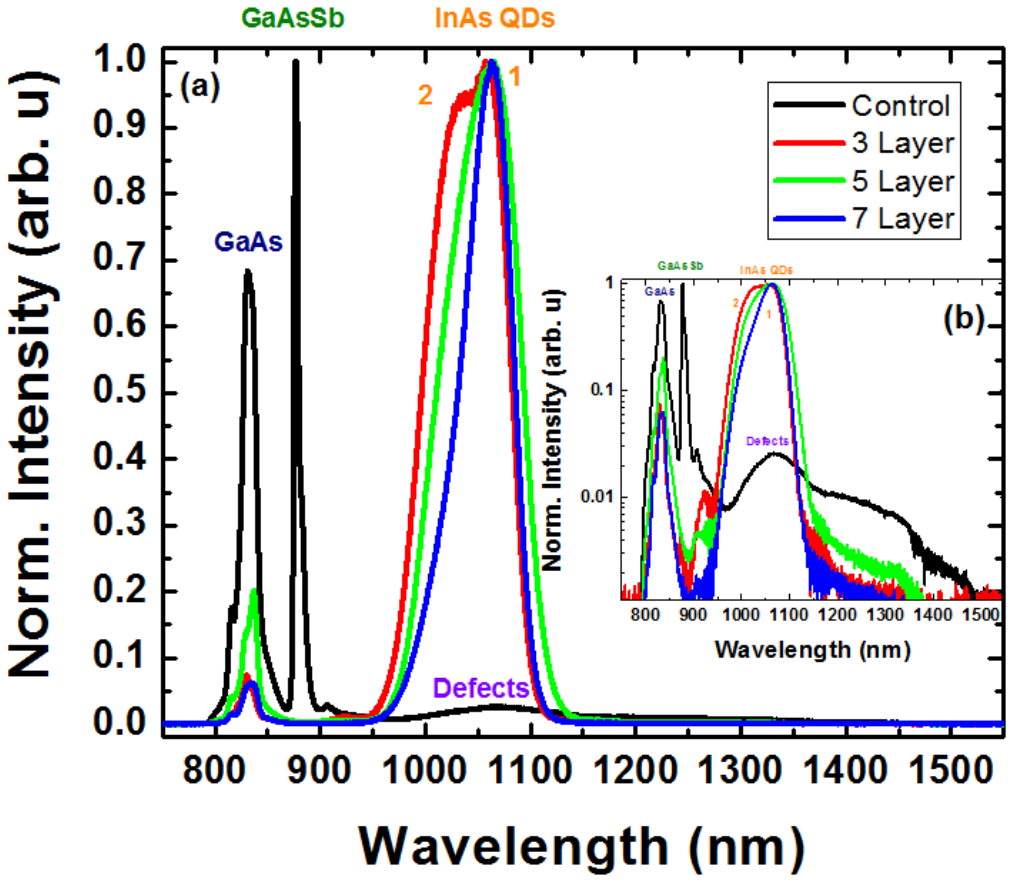



**Figure 24. 4.2 K Norm. PL with Logged Inset**
(a) shows the normalized PL spectra at 4.2 K from 700 nm to 1500 nm. Peaks and defects are labeled. QD peak is split into 2 peaks (labeled 1 and 2 for dominant peak/shoulder respectively). The inset (b) shows the same figure on a log scale. Same labels/colors are used.

At 4 K, the 3, 5, and 7 layer samples in Figure 24 (a) all show transitions for GaAs at ~ 830 nm and the InAs quantum dots at ~ 1060 nm. There is also a small transition related to the GaAsSb matrix in these samples, and this is made slightly more obvious in the inset (Figure 24 (b)), but is small due to the dominance of the lower

energy state in these samples. The GaAs peak mirrors the control GaAs peak, albeit not as bright, with the high energy shoulder. The transition associated with the low energy PL is associated with the InAs QDs. The low energy PL also reveals some other information. Each of the QD peaks show a shoulder present (labeled 2) in the logged inset of Figure 24 in (b). Additionally, the QD samples have decreasing line width with increasing layers of QDs with the 7 layer sample having the narrowest full width half maximum of the three samples measured. This could be because of bimodality in the dots as shown in additional figures showing power dependence and accompanying peak information in Figures 25 and 26 and the TD PL shown Figure 30. Bimodality, different sets of QD competing ensembles, can be the result of several different mechanisms related to non-optimum growth [43]. One such possibility is strain fields between QD layers resulting in larger QDs in the upper layers [43]. This is possible in all of the samples since each one has multiple layers allowing for large strain accumulation with relatively narrow spacing [43]. The peak for the 3 layer sample shown in the normalized PL is the most obvious bimodal of all the samples, as this sample has a second peak of comparative size. This additional peak is evident but lower in the 5 and 7 layered samples.

Figure 25 shows the power dependence for all the samples. The QD PL is also consistent with bimodal behavior as the intensity ratio of the peaks is similar with increasing power [43]. With increasing number of QDs layers the peak labeled 1 in Figures 25 (b-d) begins to dominate. This suggests that the upper QD layer becomes more uniform as the QD size gets larger [43].

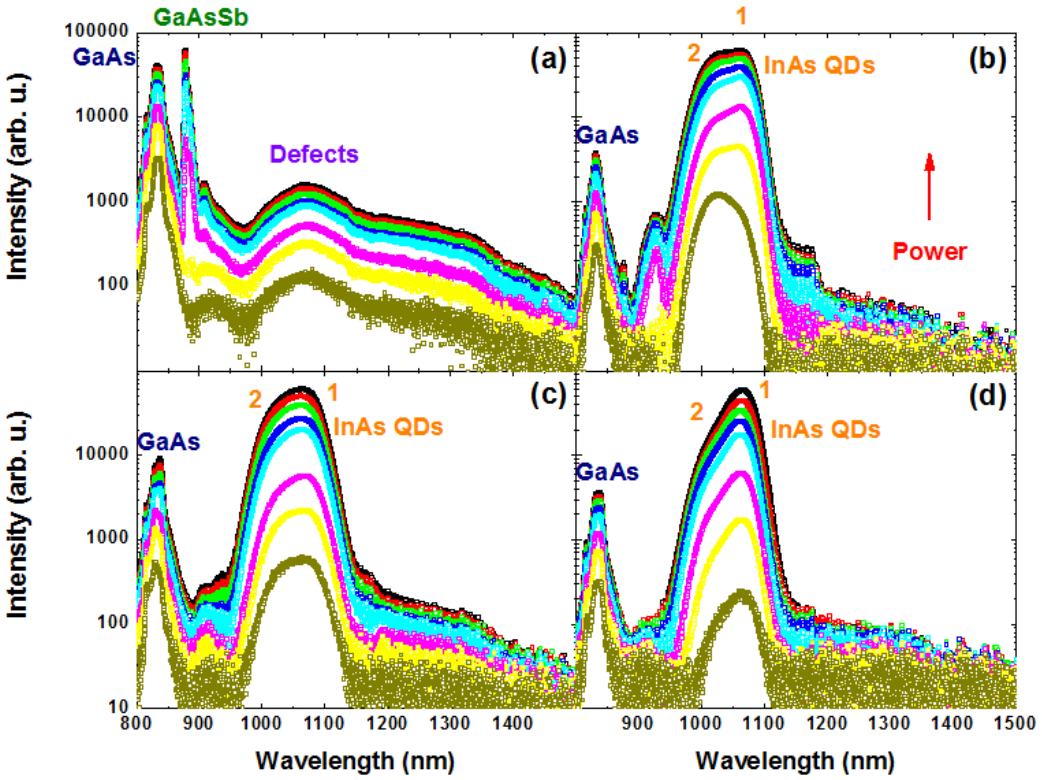



**Figure 25. 4.2 K Logged Power Dependence**
PL spectra is shown for the control (a), 3 layer (b), 5 layer (c), 7 layer (d) with increasing power going up. The peaks/defects are labeled. QD peak is split into the dominant peak and shoulder.

Power dependence can also reveal information concerning the band alignment of the system. It has been shown previously that varying the Sb from 10% to 18% will show a shift from type-I band alignment to type-II band alignment at approximately 14% Sb [34] [35] [41]. The samples studied here are also 14% Sb and therefore should show type-II band alignment. Figure 26 shows the peak energy as a result of excitation power to the cubed power. A linear relationship is shown from 0.025 $mW^{1/3}$ to 0.200 $mW^{1/3}$. This blueshift in energy upon excitation is a result of the triangular bending of the bands at the extrema of the VB and CB since carriers are in the lowest possible energy state [34] [44] [45]. It should be noted that at the lowest and highest power, the

data loses its type-II linearity: although the origin of this behavior is unknown, there are a few potential possibilities to describe this behavior: One is due to alloy fluctuations in the material as shown in a previous sample [34]. It is also possible that the carriers are either not filling in the triangular well, in the case of low power, or oversaturating the well in the case of high power. Figure 27 [34] shows the band alignment of the sample with a degenerate VB at 14% Sb. The flat VB is desirable for the system since it simplifies the IB configuration and improves hole extraction and mobility [34]. This *quasi*-type-II band alignment also increases the radiative lifetime by facilitating a greater possibility of two photon processes due to the reduced radiative recombination losses [46].

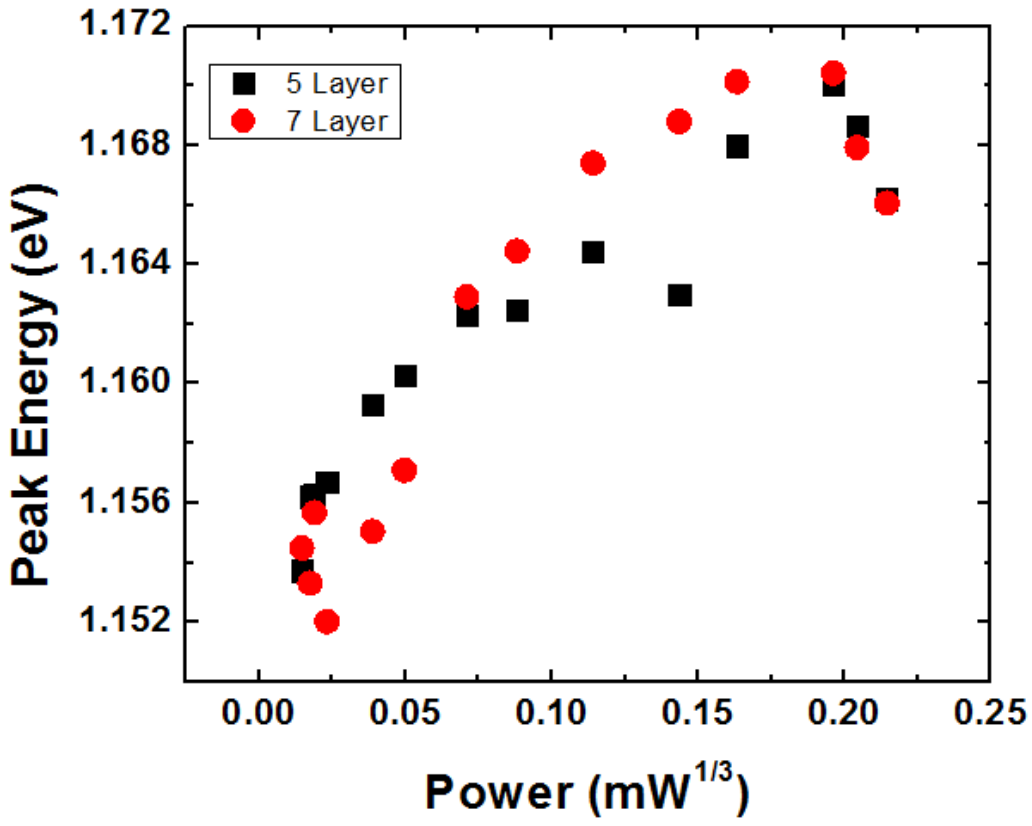



**Figure 26. PD Peak Energy vs Power$^{1/3}$**
Peak energy for the 5 and 7 layer QD sample plotted as a function of excitation power$^{1/3}$

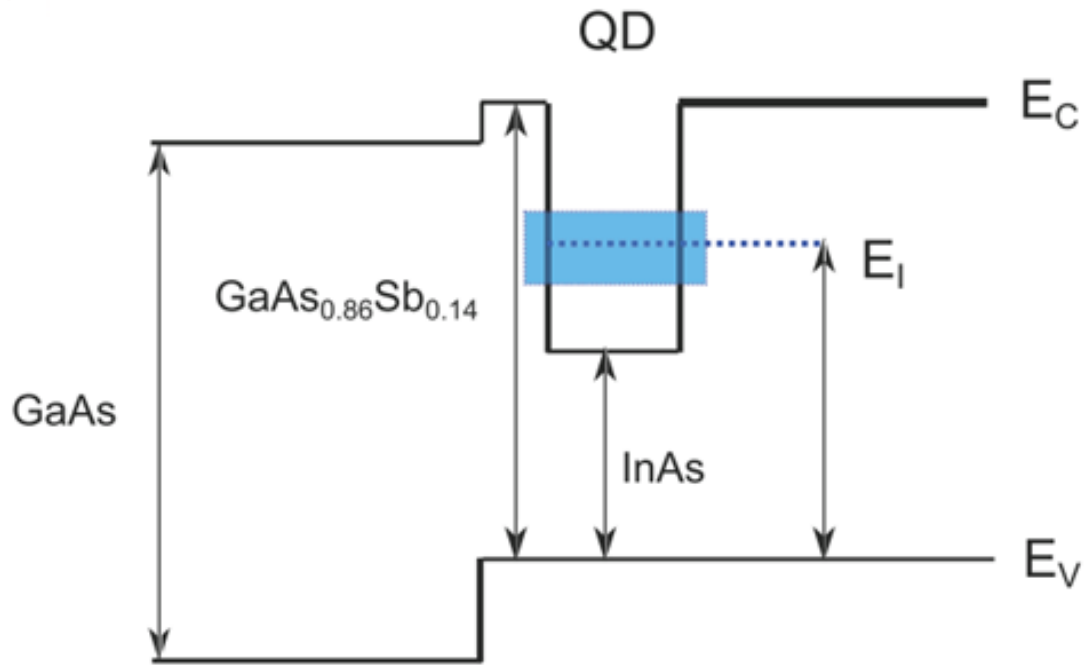



**Figure 27. Band Alignment of QD Samples**
Band alignment of our material system. InAs QD confinement (shown here in blue) represents the IB and is denoted $E_I$.

*Low-temperature External Quantum Efficiency*

Figure 28 shows EQE at 77K in two forms with plot (a) showing the linear EQE and the inset (b) showing the semi-logged plot. The control sample shows carrier extraction from the two materials present in the sample – GaAs (~ 870 nm), and GaAsSb (~900 nm). GaAs contributes the most to EQE in all cases since it comprises the bulk of the cell. The maximum EQE for the control is at ~ 37 % for GaAs, which is similar to samples previously grown and analyzed at OU [34]. This is lower than expected from high quality GaAs, which is around 80%. The reduction in total EQE observed is likely caused by poor material quality induced by strain from the 10% lattice mismatch between GaAsSb and the GaAs substrate [40]. The GaAsSb

contribution is evident from 850 nm to 900 nm, which is consistent with the PL at 4.2 K showing a peak at 875 nm.

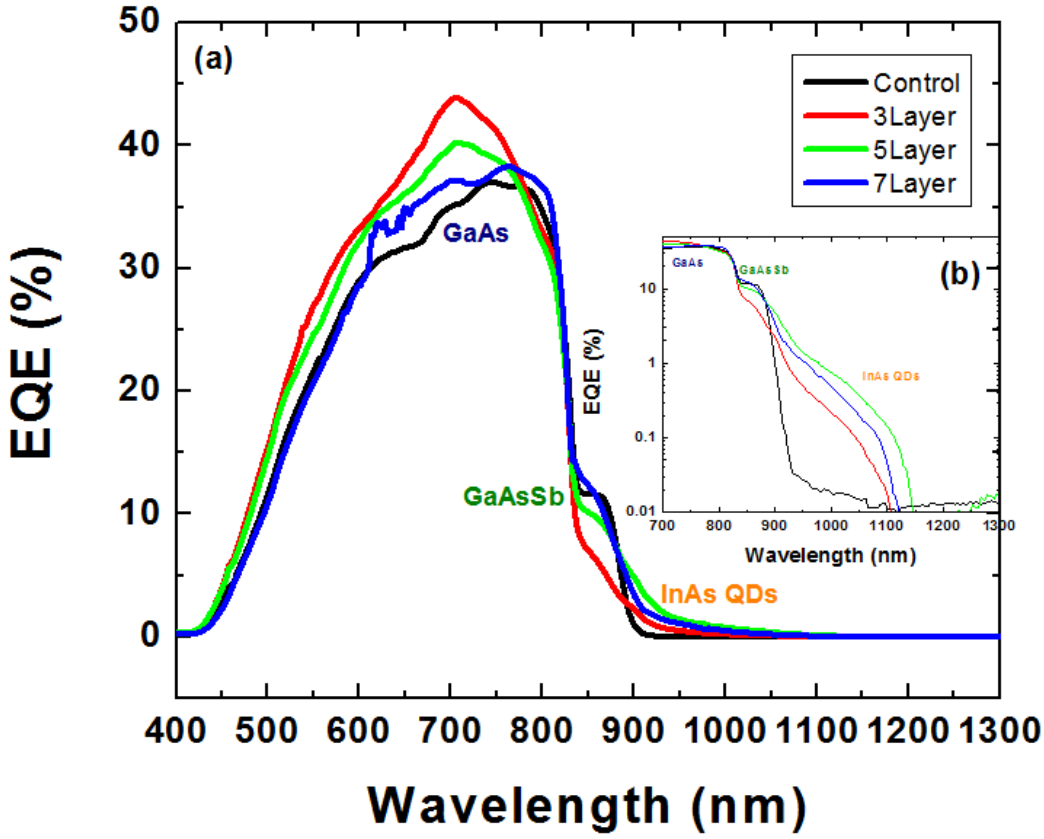



**Figure 28. EQE 77 K**
(a) shows the EQE at 77 K. Labels indicate region from where extraction takes place. (b) shows the logged EQE data at this same temperature.

The 3, 5, and 7 layer samples are also dominated by the GaAs and GaAsSb with a long wavelength contribution for the QDs. GaAs maximum EQE is low for these samples, with the 3 layer sample having the highest maximum GaAs contribution at 42% and the 7 layer exhibiting the least amount.

The GaAsSb transition isn't as obvious in the samples with dots in that each dot sample has more of a shoulder here rather than the leveled curve of the control sample.

This is due to the convolution and coupling of this transition to the QD states, which are absent in the control sample. The relative contribution of the EQE and PL at these energies agree in that the 3 layer sample with the weakest extraction or EQE corresponds to the greatest PL intensity.

Despite strong quantum confinement enhancing the PL, the carriers are not completely localized in the QDs even at low temperatures since there is evidence of carrier extraction – or non-zero EQE - in the low energy (long wavelength) region of the cell where confinement is expected to be stronger [34]. Carrier extraction here does not follow the same trend as the GaAsSb in that additional layers do not result in a larger EQE. The 5 layer sample has the largest EQE at low energies despite what should be an increase in absorption due to an increase in layers with the 7 layer sample. Since the absorption from the QDs should scale, the reason for this low total EQE is unclear. However, a reduction in the defects, or increase in the QD quality may explain this behavior since any defect-mediated extraction – and therefore enhanced carrier escape - could be reduced in high quality samples. This requires further analysis.

There are several possible extraction routes for carriers from the QDs. The first is two photon absorption. This is the ideal case for the system since for an isolated band, since this must be the mechanism through which carriers reach the conduction band without coupling the QDs to the continuum therefore avoiding any decrease in $V_{oc}$, enabling IB operation and high efficiency operation [22] [25] [47] [48]. Although, this is possible due to low energy photons in our samples, it is unlikely since competing recombination processes and non-radiative losses still dominate due to the non-optimum growth conditions in the current systems. Doped InAs QDs would increase these

chances as carrier lifetime is a function of carrier concentration [11], but the QDs here are nominally intrinsic. Thus far, this process in IB cells is not efficient relative to the radiative recombination and non-radiative processes even in well-developed InAs/GaAs due to these losses [25] [49] [50].

The second scenario to describe how carriers are contributing to EQE at low temperature is that hole extraction is contributing to the EQE at this energy because of the flat VB. Indeed, at low temperature, this is the primary source of carrier extraction due to the lack of a sizeable barrier to hole mobility.

The third possibility that is dominant in all but the coldest temperatures is that the carriers are being extracted from the QDs and other low energy states caused by defect formation in the matrix induced by the strain between GaAs and GaAsSb, which has been previously discussed and shown in the low energy PL for the control sample. This enables defected mediated carrier extraction through a low energy channel for the carriers to harness in escaping the QDs [34]. This has been observed previously in non-optimum InAs QDs [34]. In reality, it is likely that a combination of mechanisms is contributing, dominated by the effects of defects.

*Temperature Dependent External Quantum Efficiency*

The TD EQE shown in Figure 29 shows an increased EQE and therefore total extraction from the low energy states associated with the QDs with an increase in temperature for all of the samples. Two photon absorption would not be significant with an increase in temperature as would hole extraction under flat band conditions as there is either a small or no barrier at all to their mobility. Defect extraction, however, would be increased if the extra thermal energy excited electrons to higher defect states that

would allow escape from QDs via thermal hopping through various defect states into the CB. This idea of thermally assisted escape through defects is further validated by the increase in the dark current (Figure 36) and subsequent drop in $V_{oc}$ (Figure 34), which reflects an increase in Shockley-Hall-Reed (SRH) recombination when carriers travel through the intrinsic region or matrix. This further supports the hypothesis that defects in the GaAsSb matrix limit the device performance.

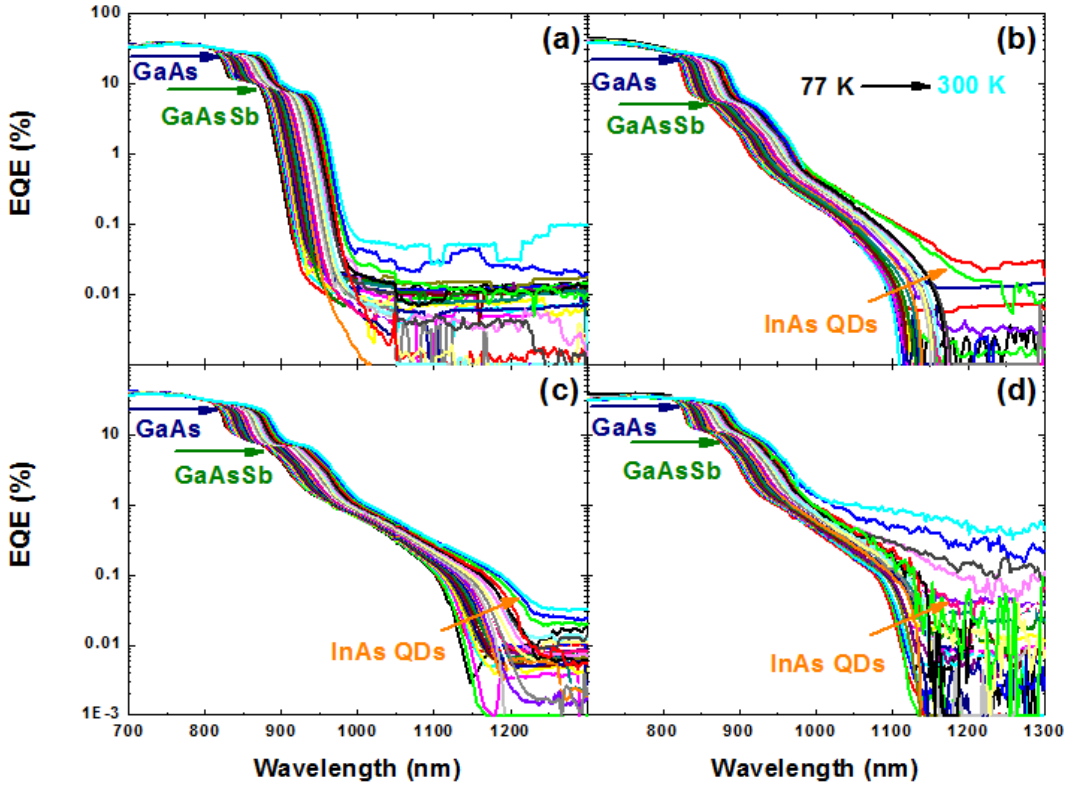



**Figure 29. Logged TD EQE**
Temperature EQE data from 77 K to 300 K for the (a) control sample (b) 3 layer (c) 5 layer (d) 7 layer. Labels indicate from where in the device extraction takes place. Arrows indicate for GaAs/GaAsSb an approximately constant EQE with an increase in temperature. Extraction from InAs QDs increases with temperature and this is noted by the orange arrow.

On inspection of TD EQE other regions of the device have less temperature dependence, notably the GaAs and GaAsSb. At these higher energies, EQE stays

relatively constant through 300 K. Thus, the amount of extraction from carriers due to GaAs/GaAsSb bands does not depend significantly on temperature. The increase in temperature does lower the band gap due to Varshni-type thermal expansion [39], but that only results in a red shift of the EQE in all regions of the device.

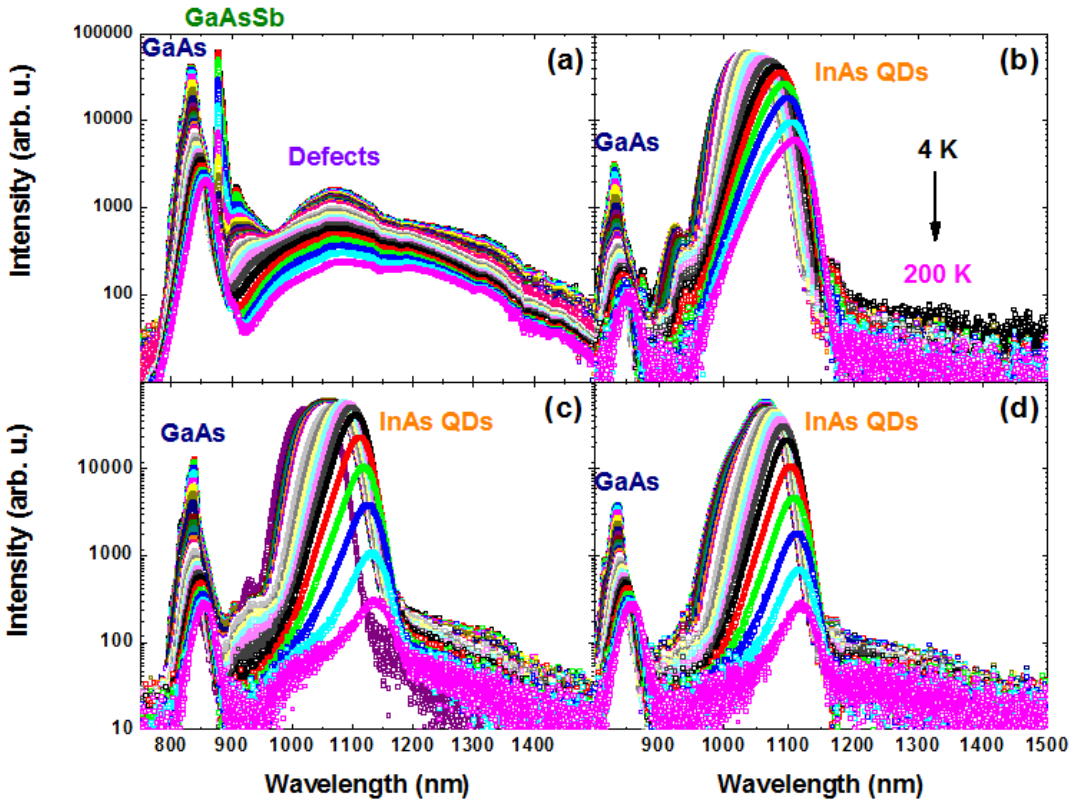



**Figure 30. Logged TD PL**
PL data from 4 K to 200 K for the (a) control sample (b) 3 layer (c) 5 layer and (d) 7 layer sample. Peaks are labeled except for the GaAsSb in the QD samples since there is no notable PL there

*Temperature Dependent Photoluminescence*

The TD PL shown in Figure 30 agrees well the EQE. First, the high energy red shifting EQE for the GaAs and GaAsSb shows up in the TD PL with these peaks each shifting in accordance to Varshni-expansion [39]. The GaAsSb peaks are difficult to extract information from in the 5 and 7 layer sample (c and d in Figure 30), but the 3

layer sample (b in Figure 30) and control sample show the normal shift in band gap for this energy as well. The PL is also consistent in that it is inversely related to increasing carrier extraction when assessing the quenching of the PL with increasing temperature. The presence of defects previously seen in low temperature PL are made apparent again in the low energy region (1060 nm) of the control sample, but this time at all temperatures. The peak energies associated with these defect or impurity states are not significantly affected by temperature.

The low energy TD PL of the QD samples is also consistent with the EQE measurements. The QD samples all show bright PL in that region at temperatures up to ~150 K in the 5 and 7 layer sample and remains bright in the 3 layer sample to over 200 K. As previously mentioned, the rate of quenching is consistent with the rate of increase of extraction in those samples. The lack of quenching in the 3 layer sample, or PL stability, may reflect the formation of smaller QDs from a reduced amount of layers; resulting in a larger confinement potential and therefore higher activation of energy in those QDs, which agrees with lower relative extraction observed in the EQE. The hypothesis that relative size of the QDs changes with an increase in layer deposition requires detailed structural analysis such as transmission electron microscopy (TEM) for confirmation. However, the relative PL energies support this hypothesis.

Figure 31 further shows the bimodality of the QDs. Instead of following the trend of decreasing peak energy and decreasing intensity with increasing temperature, the samples' PL reflects trends indicative of bimodal QDs, and thermal redistribution of carriers [51]. First, the peak energy (part (a) of Figure 31) for the 3 layer suddenly jumps at 25 K. The peak energy shift increase is indicative of a different QD population

due to thermal redistribution [43]. At low temperatures, carrier movement is limited and so they are frozen into certain localized states in the QDs. As mobility is increased, carriers escape, redistribute, and relax into a QD population more indicative of the real distribution that is higher in density and different in energy. This is seen as a peak energy shift. Additionally, the peak integration for all three QD samples increases at 75 K. This is further evidence of a thermal redistribution of carriers. This is seen as brighter PL as more carriers contribute to a single or narrower distribution. The 7-layer sample, in addition to having the narrowest FWHM, has an integrated intensity that is similar to its peak intensity implying a more uniform population of QDs. Therefore, while all three QD samples display evidence of bimodality, the 7 layer sample appears to have the most uniform population.

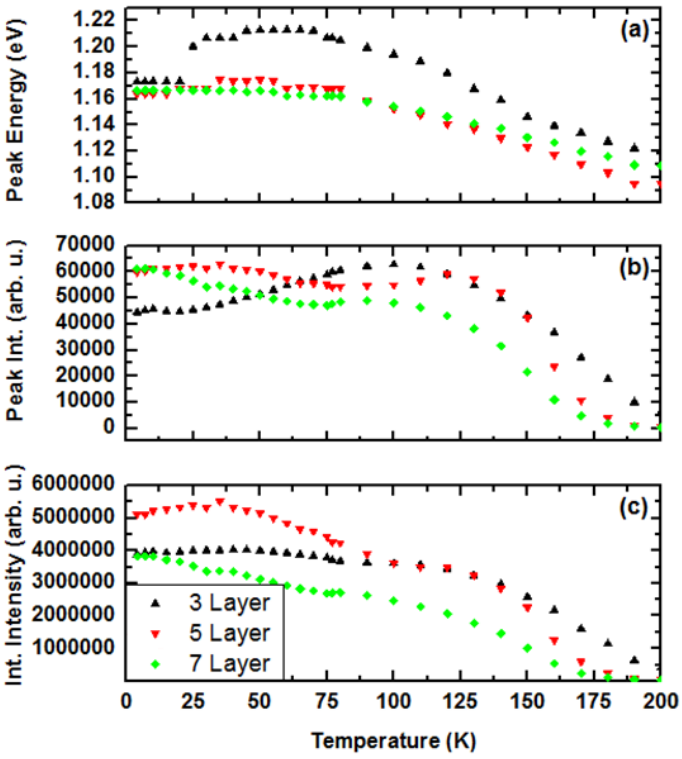



**Figure 31. Peak Data for Layered Samples**
Peak data plotted vs temperature arranged by peak energy (a), peak intensity (b) and integrated intensity (c) for the 3, 5 and 7 layer samples.

*Current Density-Voltage Analysis*

The previous measurements influence device performance, but to get a better picture of the device as a whole, current density-voltage (*J-V*) measurements were taken. Figure 32 shows the *J-V* device characteristics taken at 77 K. A large open circuit voltage is observed for the control cell in both the dark at ~1.15 V and under one Sun illumination at ~1.2 V. This represents the quasi-Fermi separation of the GaAs. The QD samples all show smaller open circuit voltage with respect to the control sample when measured under one Sun illumination. The 3 and 5 layer samples were measured as having roughly 1.1 V and the 7 layer was measured as having even less at 1.05 V at 1-sun illumination. InAs QDs in this type of system has been shown to reduce the band gap slightly [24] and this material system is no exception.

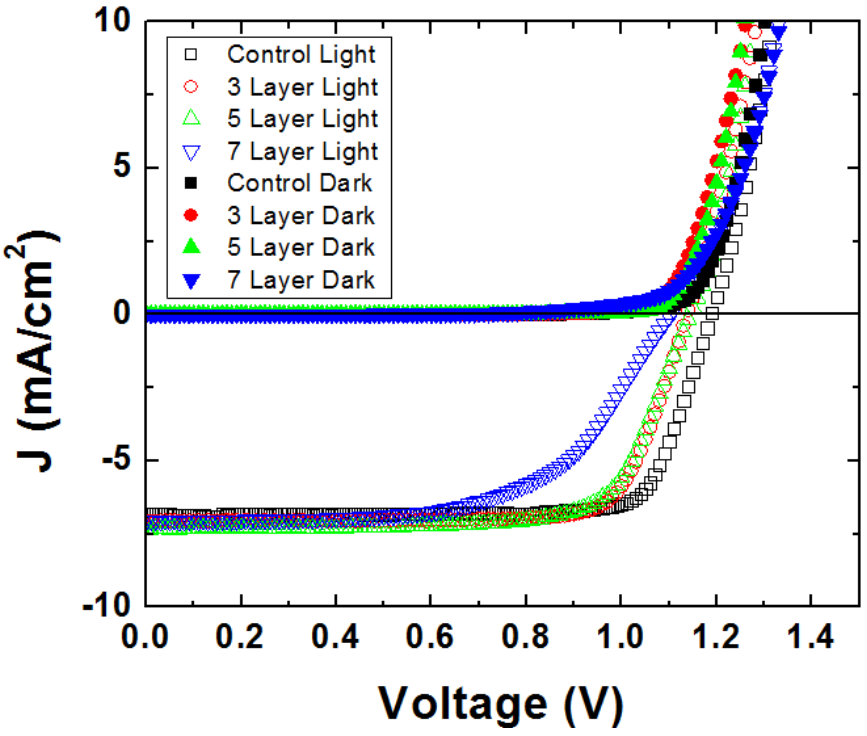



**Figure 32. 77 K J-V**
All 4 samples current density (*J*) plotted against applied bias (*V*) at 77 K in both the light (denoted by empty shapes) and dark (filled shapes). High resistances (shunt and series) can be seen in the 7 layer (light) sample reducing performance. High open circuit voltage can be seen.

Different current paths also become apparent in Figure 32. The most obvious is the shunt path at low forward biases in the 7 layer sample that reduces the overall efficiency of that device [11]. This sample also has strong series resistance due to the contacts, which can also affect the efficiency [11]. In the *light J-V* data, $J_{sc}$, the short circuit current density, increases due to the presence of QDs contributing additional absorption and extraction of additional carriers in all the samples, with the 5-layer having the largest $J_{sc}$. As stated previously, $J_{sc}$ is reflected in the EQE [11], and, since the 5-layer has the best overall EQE, this is consistent with the largest $J_{sc}$ being produced for that sample.

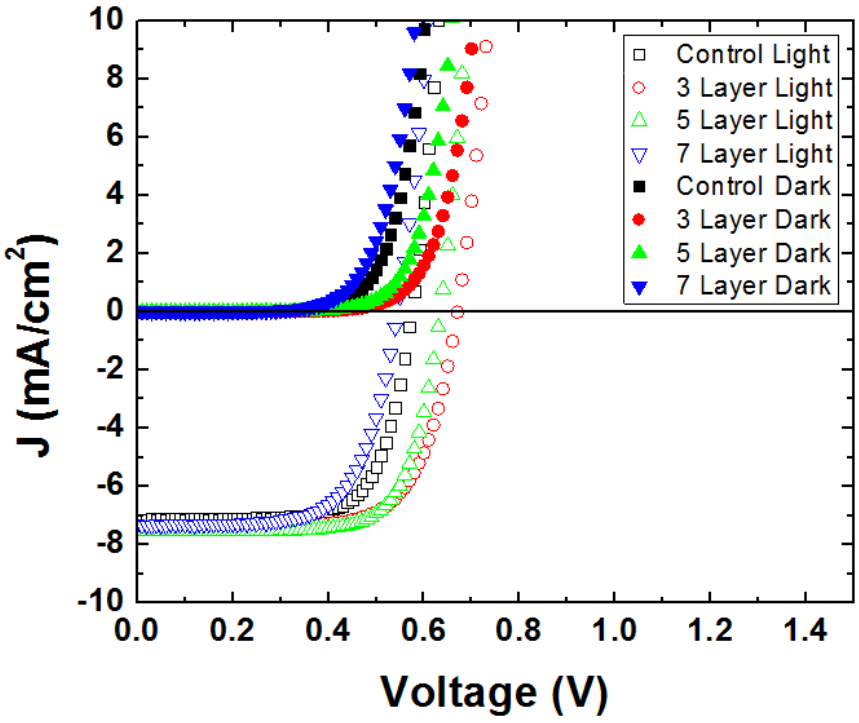



**Figure 33. 300 K J-V**
Current density (*J*) as a function of applied bias (*V*) data plotted at 300 K. Both dark (filled shapes) and light data (empty shapes) can be seen here. Reduced resistances in 7 layer due to an increase in temperature is shown, though a voltage drop from 77 K can be seen in the reduced open circuit voltage of the samples.

The resistances noted in the 77 K *J-V* data mostly vanish at 300 K as seen in Figure 33. This is typical behavior since the carriers have higher thermal energy at higher temperatures facilitating mobility. What is also reduced is the $V_{oc}$. This suggests a collapse of the quasi Fermi separation of the material and strong thermal coupling of the QD states to the matrix (continuum) in agreement with previous discussions with respect to thermally activated carriers escaping the QDs [22] [34]. To an extent, with an increase in temperature, the voltage drops, but not this drastically and at most should be 0.05 to 0.1 V [39]. The 3-layer sample has the highest band gap at almost 0.6V, which agrees with the higher activation energy of the carriers from the QDs determined for this sample. Lastly and most importantly: the control sample also experiences this large $V_{oc}$ drop. The $V_{oc}$ is summarized in Figure 34.

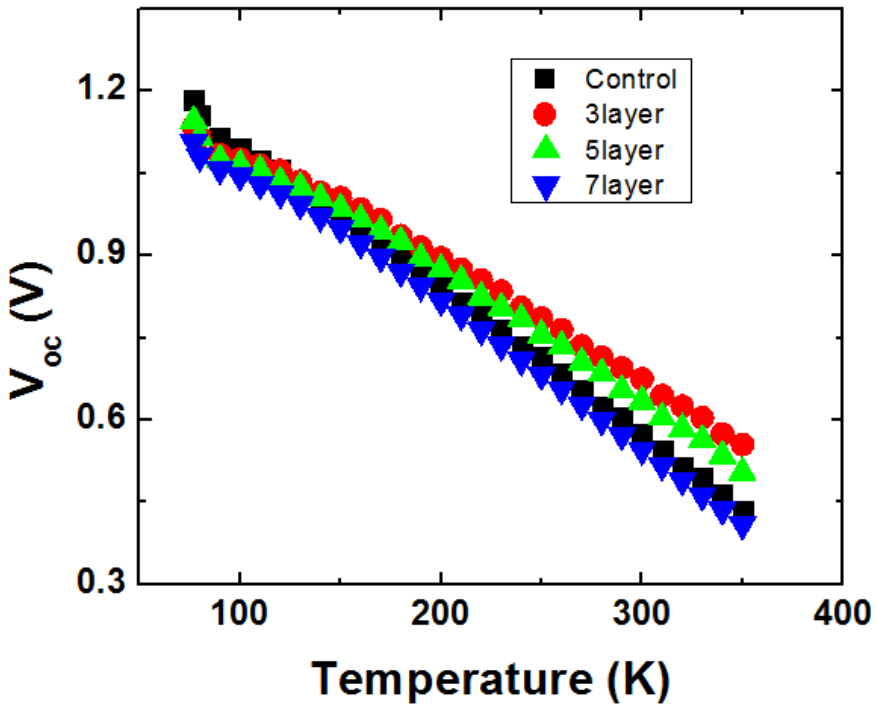



**Figure 34. Temperature Dependent $V_{oc}$**
$V_{oc}$, open circuit voltage, plotted as a function of temperature for each the samples plotted here. All samples experience a drastic drop in open circuit voltage relative to the ~0.1 V due to thermal expansion of the material

*Open-circuit Voltage Analysis*

The $V_{oc}$ drop observed in Figure 34 is dominated by the effects defects induced by the lattice mismatch between GaAs and GaAsSb and the subsequent strongly correlated increase in dark current. This becomes an obvious conclusion because this is seen in the control sample. The defects, seen in the PL of the control sample, are prevalent not just in the control sample, but all the samples as indicated by the simultaneous increase in carrier escape from the dots from the EQE and the large increase in the dark current at elevated temperatures.

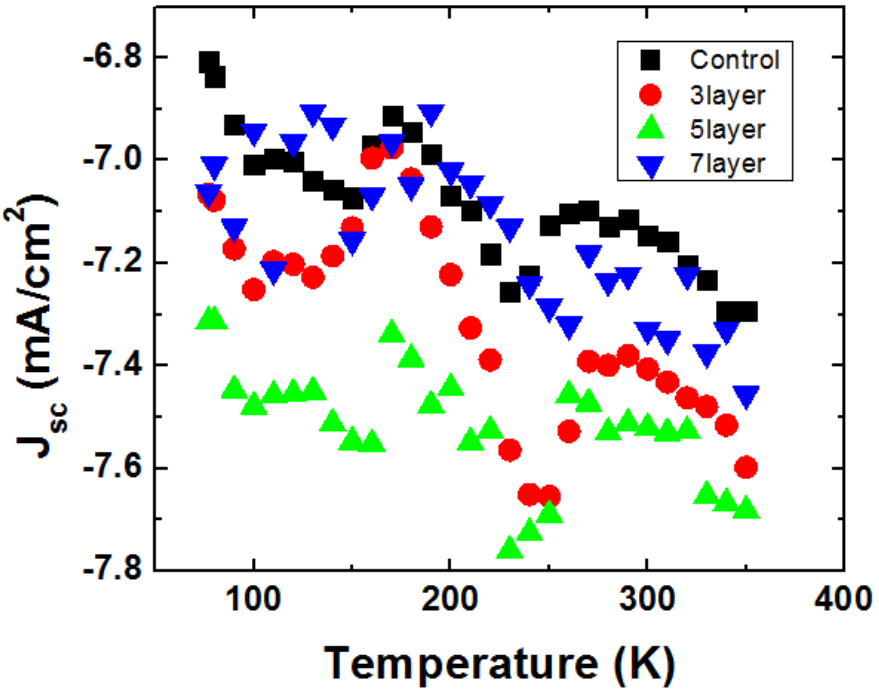



**Figure 35. Temperature Dependent $J_{sc}$**
$J_{sc}$ is plotted against temperature for each of the samples. This data follows an untypical trend as $J_{sc}$ does not just increase with temperature as expected but also decreases. This is thought to be due to nonradiative recombination due to defects within the material.

*Short-circuit current Analysis*

In general, $J_{sc}$ increases with increasing temperature because an increase in temperature results in a larger absorption of light due to a decreasing band gap as a result of Varshni-type thermal expansion [39]. The general trend in each of the samples here still results in an increase, but with an unusual decrease at T > 180 K followed by a sharp increase until 230 K, followed by a further decrease until 280 K. This odd behavior has been measured consistently across multiple samples discussed in this thesis and in another set of samples grown at OU for the same material system [34]. The thought is that this behavior is linked to subtle competition between radiative, non-radiative recombination, and the relative kinetic energy of the carriers upon activation and escape from the QDs. This is a noted problem in IBSC solar cells but exacerbated here by defect formation [22]. As carrier extraction increases due to increasing temperature and defect mediated escape, some carriers that get excited to the CB are lost to additional defects as they are transported through the matrix; resulting in non-radiative recombination, which reduces $J_{sc}$ at different temperatures. This also has the effect of significantly decreasing $V_{oc}$ as illustrated in Figure 34.

*Temperature dependent dark current-voltage Analysis*

Figure 36 shows the temperature dependent semi-logged dark (under no illumination) *J-V* measurements. Each sample shows two (or more) diode-like characteristics at low temperature. This is evident through an additional resistive path observed as inflection points at lower voltages in Figure(s) 36 (a-d). The possible mechanisms for these paths are described and shown in Figure 16 and equation 7. As the temperature increases, the additional energy results in data that reflects a single

diode, screening the lower temperature perturbation of carrier transport within the sample. Each of the samples show only one barrier, except for the 3 layer sample. This samples bimodality results in two (or several) barriers as illustrated in Figure 36 (c) with one at 0.6 V and the other at roughly 1.1 V at the lowest temperature.

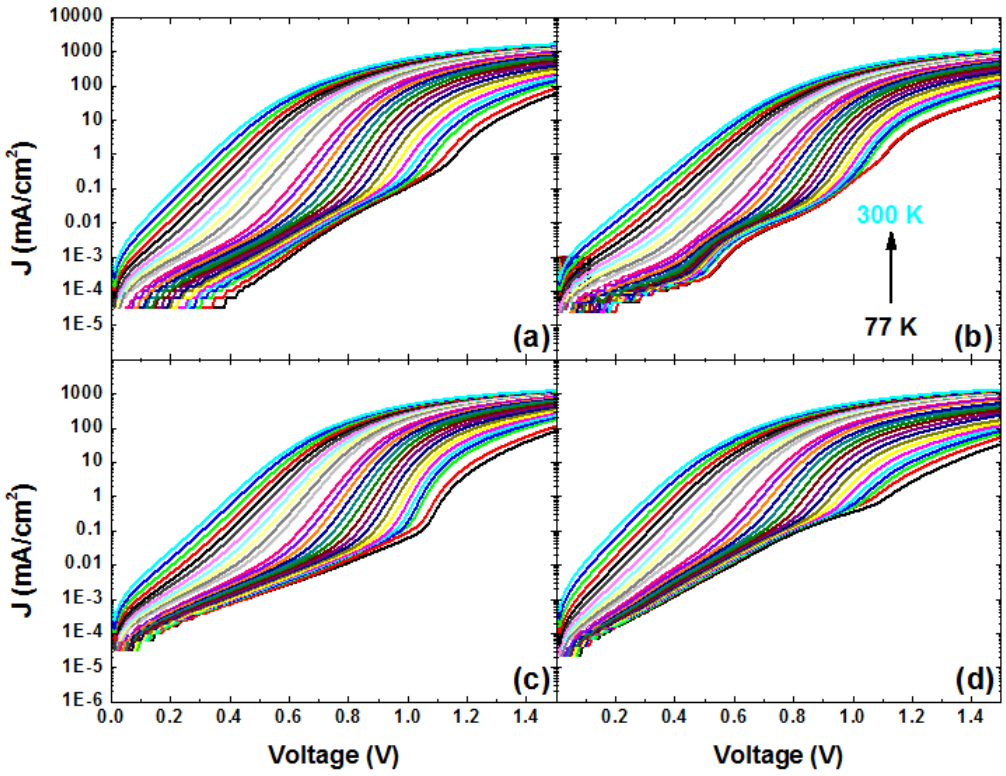



**Figure 36. Temperature Dependent Jdark-V Measurements**
Dark saturation current is plotted here as a function of applied bias in a semilog scale for the (a) Control (b) 3 layer (c) 5 layer (d) 7 layer. The data shows multiple diodes due to varying current paths within the material at lower temperatures. These paths vanish at higher temperatures which reflects single diode behavior.

As a way to further understand the complicated transport properties of the dark *J-V* measurements, fits were performed using the aforementioned Williams-model [42] as described by equation 7. An example of the fits produced is shown in Figure 37. The model works well at higher temperatures. At low temperatures (100 K or below) when

the complexity of the structure in the *J-V* data is at a maximum, the model becomes less ideal (particularly) in the higher bias regime (> 1.0 V).

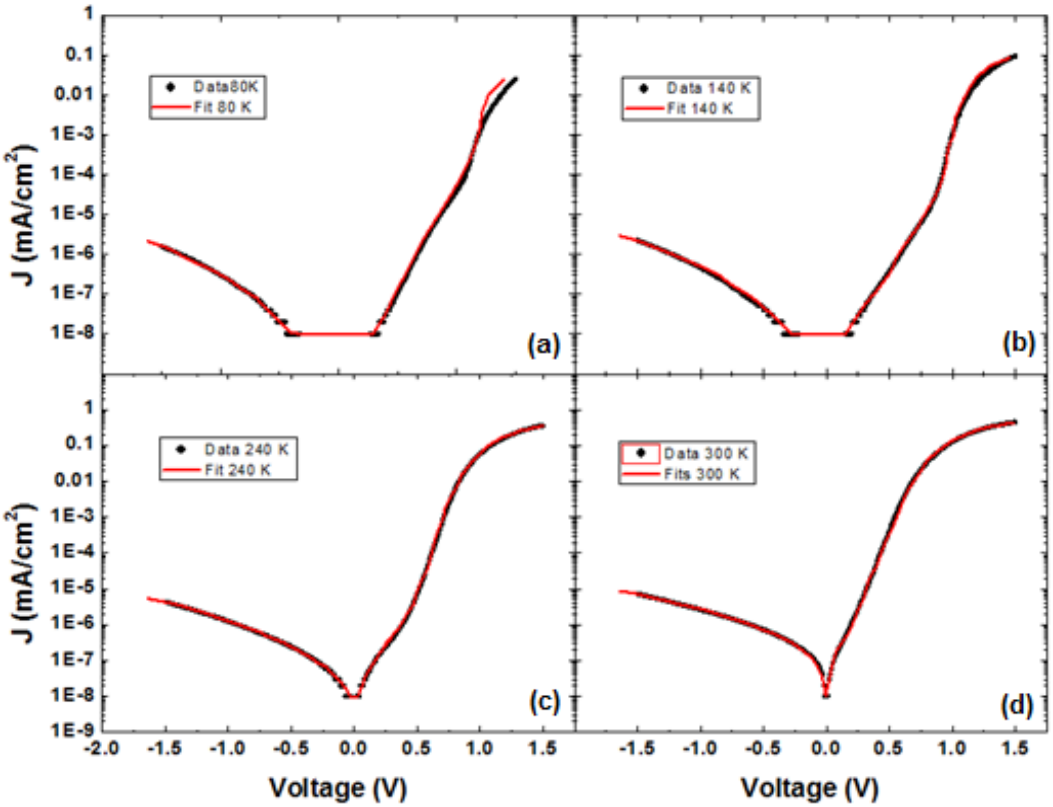



**Figure 37. Example of Fits in Control**
Results of fits as examples are shown for four temperatures (a) 80 K, (b) 140 K, (c) 240 K, (d) 300 K. Fitting becomes less accurate at low temperatures due to additional current paths not accounted for in the model.

From these fits, different parameters can be extracted as mentioned in equations 8, 9 (shown again for convenience).

$$J_{01} = J_{001} T^2 e^{\frac{-\Delta E}{nK_B T}} \quad \textbf{(10)}$$

$$J_{02} = J_{002}e^{BT} \quad \textbf{(11)}$$

The most important of these are the two dark currents – $J_{01}$ and $J_{02}$ since they can be used to extract information regarding the dominant transport processes and barrier to carrier extraction that results. These are shown in Figure 38.

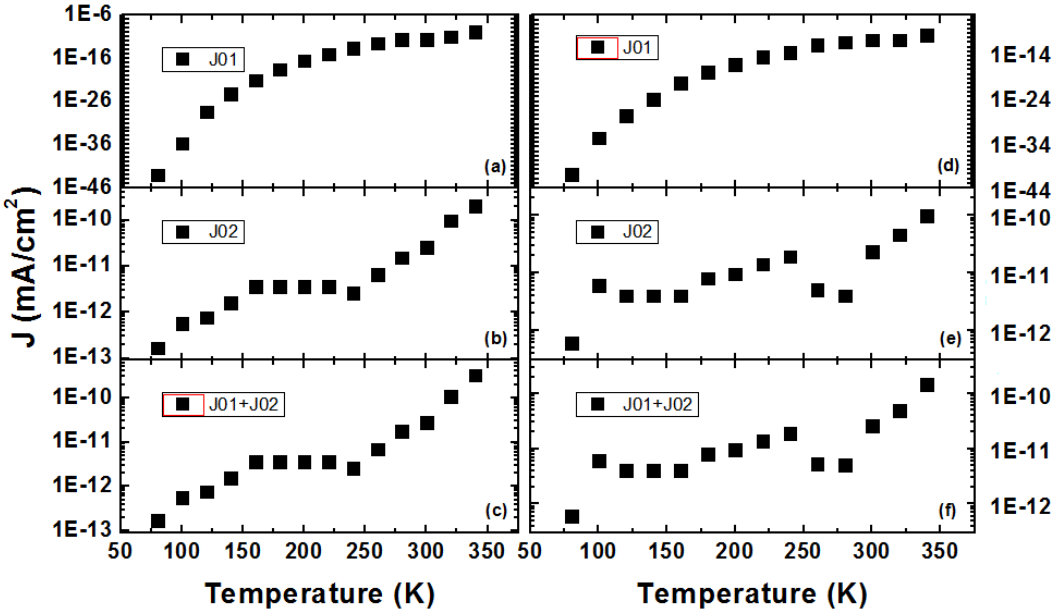



**Figure 38. Dark Saturation Current Coefficients**
$J_0$ results from fits plotted as a function of temperature. (a) – (c) are the control sample while (d) – (f) are from 5 layer sample. The second diode dominates the dark saturation current in both samples.

In both samples, the dark current is a result of two diodes plus other parasitic resistive paths. Diode one, $J_{01}$, even at the highest temperatures, still has a fairly low current of $10^{-12}$ mA/cm$^2$. Diode two, $J_{02}$, however, has a larger current on the order of two magnitudes higher. This means that this diode dominates the dark current behavior at all temperatures as shown in the combination of their currents in the figures.

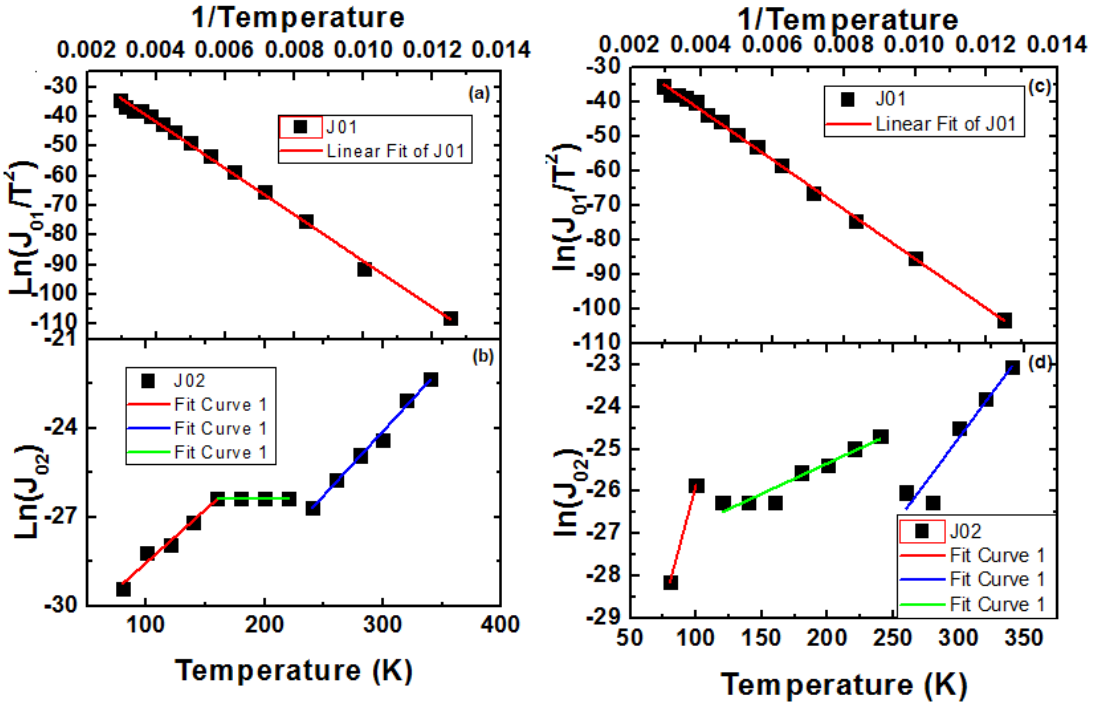



**Figure 39. Barrier Extraction of Dark Currents.**
Fits for the dark saturation current data in figure 38. (a) and (b) show the fits for the control sample while (c) and (d) show the fits for the 5 layer sample. (a) and (c) are believed to be due to the main junction due to the Arrhenius plot fitting $J_{01}$. (b) and (d) are the fits for the second diode, $J_{01}$ believed to be a tunneling diode. The rise, stay constant, rise, can be seen as a "knee" in the $V_{oc}$, but this still requires further investigation.

The left fits in Figure 39 show in both the control sample and 5 layer sample, the first diode is dominated by diffusion and recombination based on the fit to equation 8. This diode is related to the main junction of the solar cell, and represents the generation-diffusion transport of the minority carriers traversing the intrinsic region. Diode two, however, is attributed to carrier localization at lower temperature in the QDs and subsequent escape via tunneling and thermal activation based upon the fit to equation 9. Each sample seems to have two (or more) barriers shown as different slopes in Figure(s) 39 (red, green, blue) suggesting that the transport is limited by two or more barriers at different temperatures, which correlates with the large $V_{oc}$ reduction observed in Figure

34. There is a slight knee in the $V_{oc}$ data (in most samples) before 150 K and this is where the second diode fits level off, or become more uncertain. The fact that this is attributed to tunneling with two (or more) different barriers to transport, agrees with statements above discussing defect mediated escape, as observed previously in QDSCs [46]. Tunneling itself is a temperature *independent* mechanism [44] but the point at which a carrier can tunnel through the system is dependent on temperature as shown through the EQE and PL measurements. The material system has several defect sites due to defects induced by the 10% mismatch between GaAs and GaAsSb and QDs. Once a carrier has enough kinetic (thermal) energy to reach these defect levels, the potential barrier becomes less, and tunneling becomes more likely [44]. These routes contribute to an increase in dark current, which aids in the collapse of the $V_{oc}$. The introduction of dots as seen in the 5-layer sample reduces the total strain of the system since some of the surface energy is transferred to spontaneous QD formation, lowering the potential for the production of defects; so, reducing defect-related tunneling sites, while increasing the confinement and activation of carriers in the QDs until higher temperatures.

# Chapter 5: Conclusion

Four InAs/$GaAs_{.86}Sb_{.14}$ QD IBSCs with varying layers of QDs were analyzed in this study with a QD-free sample serving as a control. GaAsSb matrices increase InAs QD density over InAs QDs grown on GaAs and aids in hole extraction by formation of a flat VB. GaAsSb, however, also contributes to defects present in all the samples due to the lattice mismatch between GaAs and GaAsSb. These defects assist in carrier extraction from the QDs through tunneling and thermal escape, which appears to inhibit formation of a true intermediate band in these systems, especially at higher temperatures. The formation of defects, along with large temperature dependent dark current contributes to the collapse of the $V_{oc}$ through coupling of the QDs to the matrix and increased SRH recombination. Additionally, defects also contribute to non-radiative recombination, which reduces $J_{sc}$. As such, currently some mechanisms important to IBSC operation, such as an isolated IB and two photon absorption remain limited. Further measurements, such as those that use two excitation sources, would be helpful in determining the presence of an isolated IB and the rate of two photon absorption in these systems. A comprehensive material analysis is also required to directly assess the nature of QD formation and the rise of defects in these structures.

# References


[1] 2015 Key World Energy Statistics, 1st ed. Paris: IEA Publishing, 2015, p. 6.

[2] "coal power: air pollution", Union of Concerned Scientists. [Online]. Available: http://www.ucsusa.org/clean_energy/coalvswind/c02c.html#.Vy4cnb5LlmM. [Accessed: 05- Apr- 2016].

[3] M. Prasad and K. Kumari, "Toxicity of Crude Oil to the Survival of the Fresh Water FishPuntius sophore (HAM.)", Acta hydrochim. hydrobiol., vol. 15, no. 1, pp. 29-36, 1987.

[4] Understanding and Responding to Climate Change: Highlights of National Academies Reports, 1st ed. Washington, D.C.: National Academies Press, 2008, pp. 5-10.

[5] L. Bernstein, P. Bosch, O. Canziani and Z. Chen, Climate Change 2007 - Synthesis Report: A report of the Intergovernmental Panel on Climate Change, 1st ed. Geneva: Intergovernmental Panel on Climate Change, 2008, pp. 58-60.

[6] World Energy Assessment: Energy and the Challenge of Sustainability., 1st ed. New York: UNDP, 2000, pp. 236-237.

[7] Solar Energy Perspectives, 1st ed. France: IEA Publications, 2011, pp. 23, 31.

[8] The Future of Solar Energy: An Interdisciplinary MIT Study, 1st ed. Massachusetts Institute of Technology, 2015, p. xiii-xviii, 80.

[9] "NREL: Energy Analysis - Levelized Cost of Energy Calculator", Nrel.gov, 2016. [Online]. Available: http://www.nrel.gov/analysis/tech_lcoe.html. [Accessed: 13- May- 2016].

[10] The History of Solar, 1st ed. pp. 1-12.

[11] J. Nelson, The physics of solar cells. London: Imperial College Press, 2003.

[12] PHOTOVOLTAICS REPORT, 1st ed. Frieburg: Fraunhofer Institute for Solar Energy Systems, ISE, 2016, pp. 19-20.

[13] D. Bradsher, "Chinese Firm Buys an American Solar Technology Start-Up", Nytimes.com, 2013. [Online]. Available: http://www.nytimes.com/2013/01/10/business/energy-environment/chinese-company-buys-2-solar-companies-from-west.html?_r=0. [Accessed: 05- Apr- 2016].

[14] "Research | First Solar", Firstsolar.com, 2016. [Online]. Available: http://www.firstsolar.com/en/About-Us/Research. [Accessed: 05- Apr- 2016].

[15] M. Green, Third generation photovoltaics. Berlin: Springer, 2006.

[16] W. Shockley and H. Queisser, "Detailed Balance Limit of Efficiency of p-n Junction Solar Cells", J. Appl. Phys., vol. 32, no. 3, p. 510, 1961.

[17] G. Conibeer, "Third-generation photovoltaics", Materials Today, vol. 10, no. 11, pp. 42-50, 2007.

[18] V. Whiteside, The optical Aharonov-Bohm effect and magneto-optical properties of type-II quantum dots. 2011.

[19] L. Hirst and N. Ekins-Daukes, "Fundamental losses in solar cells", Prog. Photovolt: Res. Appl., vol. 19, no. 3, pp. 286-293, 2010.

[20] J. Tang, V. Whiteside, H. Esmaielpour, S. Vijeyaragunathan, T. Mishima, M. Santos and I. Sellers, "Effects of localization on hot carriers in $InAs/AlAs_xSb_{1-x}$ quantum wells", Appl. Phys. Lett., vol. 106, no. 6, p. 061902, 2015.

[21] H. Esmaielpour, V. Whiteside, J. Tang, S. Vijeyaragunathan, T. Mishima, S. Cairns, M. Santos, B. Wang and I. Sellers, "Suppression of phonon-mediated hot carrier relaxation in type-II $InAs/AlAs_xSb_{1-x}$quantum wells: a practical route to hot carrier solar cells", Prog. Photovolt: Res. Appl., vol. 24, no. 5, pp. 591-599, 2016.

[22] A. Luque and A. MartÃ-, "The Intermediate Band Solar Cell: Progress Toward the Realization of an Attractive Concept", Adv. Mater., vol. 22, no. 2, pp. 160-174, 2010.

[23] G. Jolley, H. Lu, L. Fu, H. Tan and C. Jagadish, "Electron-hole recombination properties of $In_{0.5}Ga_{0.5}As/GaAs$ quantum dot solar cells and the influence on the open circuit voltage", Appl. Phys. Lett., vol. 97, no. 12, p. 123505, 2010.

[24] I. Ramiro, A. Marti, E. Antolin and A. Luque, "Review of Experimental Results Related to the Operation of Intermediate Band Solar Cells", IEEE Journal of Photovoltaics, vol. 4, no. 2, pp. 736-748, 2014.

[25] A. Martí, E. Antolín, C. Stanley, C. Farmer, N. López, P. Díaz, E. Cánovas, P. Linares and A. Luque, "Production of Photocurrent due to Intermediate-to-Conduction-Band Transitions: A Demonstration of a Key Operating Principle of the Intermediate-Band Solar Cell", Phys. Rev. Lett., vol. 97, no. 24, pp. 247701-1-4, 2006.

[26] N. López, L. Reichertz, K. Yu, K. Campman and W. Walukiewicz, "Engineering the Electronic Band Structure for Multiband Solar Cells", Phys. Rev. Lett., vol. 106, no. 2, pp. 028701-1-028701-4, 2011.

[27] D. Norris, Measurement and assignment of the size-dependent optical spectrum in cadmium selenide (CdSe) quantum dots. 1995.

[28] S. Hubbard, C. Cress, C. Bailey, R. Raffaelle, S. Bailey and D. Wilt, "Effect of strain compensation on quantum dot enhanced GaAs solar cells", Appl. Phys. Lett., vol. 92, no. 12, p. 123512, 2008.

[29] K. Sablon, J. Little, K. Olver, Z. Wang, V. Dorogan, Y. Mazur, G. Salamo and F. Towner, "Effects of AlGaAs energy barriers on InAs/GaAs quantum dot solar cells", J. Appl. Phys., vol. 108, no. 7, p. 074305, 2010.

[30] P. Simmonds, R. Babu Laghumavarapu, M. Sun, A. Lin, C. Reyner, B. Liang and D. Huffaker, "Structural and optical properties of InAs/AlAsSb quantum dots with GaAs(Sb) cladding layers", Appl. Phys. Lett., vol. 100, no. 24, p. 243108, 2012.

[31] R. Laghumavarapu, A. Moscho, A. Khoshakhlagh, M. El-Emawy, L. Lester and D. Huffaker, "GaSb⁄GaAs type II quantum dot solar cells for enhanced infrared spectral response", Appl. Phys. Lett., vol. 90, no. 17, p. 173125, 2007.

[32] S. Hatch, J. Wu, K. Sablon, P. Lam, M. Tang, Q. Jiang and H. Liu, "InAs/GaAsSb quantum dot solar cells", Opt. Express, vol. 22, no. 3, p. A679, 2014.

[33] F. Tutu, I. Sellers, M. Peinado, C. Pastore, S. Willis, A. Watt, T. Wang and H. Liu, "Improved performance of multilayer InAs/GaAs quantum-dot solar cells using a high-growth-temperature GaAs spacer layer", J. Appl. Phys., vol. 111, no. 4, p. 046101, 2012.

[34] Y. Cheng, M. Fukuda, V. Whiteside, M. Debnath, P. Vallely, T. Mishima, M. Santos, K. Hossain, S. Hatch, H. Liu and I. Sellers, "Investigation of InAs/$GaAs_{1-x}Sb_x$ quantum dots for applications in intermediate band solar cells", Solar Energy Materials and Solar Cells, vol. 147, pp. 94-100, 2016.

[35] M. Levy and C. Honsberg, "Nanostructured Absorbers for Multiple Transition Solar Cells", IEEE Trans. Electron Devices, vol. 55, no. 3, pp. 706-711, 2008.

[36] Y. Liao, W. Hsu, P. Chiu, J. Chyi and W. Chang, "Effects of thermal annealing on the emission properties of type-II InAs/GaAsSb quantum dots", Appl. Phys. Lett., vol. 94, no. 5, p. 053101, 2009.

[37] W. Liu, Y. Wang, W. Qiu and C. Fang, "Carrier Dynamics of a Type-II Vertically Aligned InAs Quantum Dot Structure with a GaAsSb Strain-Reducing Layer", Appl. Phys. Express, vol. 6, no. 8, p. 085001, 2013.

[38] J. Pankove, Optical processes in semiconductors. Englewood Cliffs, N.J.: Prentice-Hall, 1971.

[39] Y. Varshni, "Temperature dependence of the energy gap in semiconductors", Physica, vol. 34, no. 1, pp. 149-154, 1967.

[40] H. Liu, I. Sellers, T. Badcock, D. Mowbray, M. Skolnick, K. Groom, M. Gutiérrez, M. Hopkinson, J. Ng, J. David and R. Beanland, "Improved performance of 1.3 μm multilayer InAs quantum-dot lasers using a high-growth-temperature GaAs spacer layer", Appl. Phys. Lett., vol. 85, no. 5, p. 704, 2004.

[41] S. Tomić, "Effect of Sb induced type II alignment on dynamical processes in InAs/GaAs/GaAsSb quantum dots: Implication to solar cell design", Appl. Phys. Lett., vol. 103, no. 7, p. 072112, 2013.

[42] B. Williams, S. Smit, B. Kniknie, K. Bakker, W. Keuning, W. Kessels, R. Schropp and M. Creatore, "Identifying parasitic current pathways in CIGS solar cells by modelling dark J-V response", Prog. Photovolt: Res. Appl., vol. 23, no. 11, pp. 1516-1525, 2015.

[43] I. Sellers, Optimisation And Study Of 1.3μm In(Ga)As Quantum Dot Lasers. 2004.

[44] C. Weisbuch and B. Vinter, Quantum semiconductor structures. Boston: Academic Press, 1991.

[45] F. Hatami, M. Grundmann, N. Ledentsov, F. Heinrichsdorff, R. Heitz, J. Böhrer, D. Bimberg, S. Ruvimov, P. Werner, V. Ustinov, P. Kop'ev and Z. Alferov, "Carrier dynamics in type-II GaSb/GaAs quantum dots", Phys. Rev. B, vol. 57, no. 8, pp. 4635-4641, 1998.

[46] S. Willis, J. Dimmock, F. Tutu, H. Liu, M. Peinado, H. Assender, A. Watt and I. Sellers, "Defect mediated extraction in InAs/GaAs quantum dot solar cells", Solar Energy Materials and Solar Cells, vol. 102, pp. 142-147, 2012

[47] A. Luque and A. Martí, "Increasing the Efficiency of Ideal Solar Cells by Photon Induced Transitions at Intermediate Levels", Phys. Rev. Lett., vol. 78, no. 26, pp. 5014-5017, 1997.

[48] E. Antolín, A. Martí, C. Farmer, P. Linares, E. Hernández, A. Sánchez, T. Ben, S. Molina, C. Stanley and A. Luque, "Reducing carrier escape in the

InAs/GaAs quantum dot intermediate band solar cell", J. Appl. Phys., vol. 108, no. 6, p. 064513, 2010.

[49] A. Martí, E. Antolín, P. García Linares, I. Ramiro, I. Artacho, E. López, E. Hernández, M. Mendes, A. Mellor, I. Tobías, D. Fuertes Marrón, C. Tablero, A. Cristóbal, C. Bailey, M. Gonzalez, M. Yakes, M. Lumb, R. Walters and A. Luque, "Six not-so-easy pieces in intermediate band solar cell research", Journal of Photonics for Energy, vol. 3, no. 1, p. 031299, 2013.

[50] P. Lam, S. Hatch, J. Wu, M. Tang, V. Dorogan, Y. Mazur, G. Salamo, I. Ramiro, A. Seeds and H. Liu, "Voltage recovery in charged InAs/GaAs quantum dot solar cells", Nano Energy, vol. 6, pp. 159-166, 2014.

[51] H. Liu, M. Hopkinson, C. Harrison, M. Steer, R. Frith, I. Sellers, D. Mowbray and M. Skolnick, "Optimizing the growth of 1.3 μm InAs/InGaAs dots-in-a-well structure", J. Appl. Phys., vol. 93, no. 5, p. 2931, 2003.